IOP Publishing Bioinspir. Biomim. 12 (2017) 026013 https://doi.org/10.1088/1748-3190/aa60e2

Bioinspiration & Biomimetics

PAPER

Global dynamics of non-equilibrium gliding in animals

Isaac J Yeaton[1], John J Socha[2] and Shane D Ross[2]

[1] Department of Mechanical Engineering Virginia Tech Blacksburg, VA United States of America
[2] Department of Biomedical Engineering and Mechanics Virginia Tech Blacksburg, VA United States of America

E-mail: iyeaton@vt.edu

RECEIVED
8 September 2016

REVISED
31 January 2017

ACCEPTED FOR PUBLICATION
16 February 2017

PUBLISHED
17 March 2017

Keywords: gliding, equilibrium, control

Supplementary material for this article is available online

Abstract

Gliding flight—moving horizontally downward through the air without power—has evolved in a broad diversity of taxa and serves numerous ecologically relevant functions such as predator escape, expanding foraging locations, and finding mates, and has been suggested as an evolutionary pathway to powered flight. Historically, gliding has been conceptualized using the idealized conditions of equilibrium, in which the net aerodynamic force on the glider balances its weight. While this assumption is appealing for its simplicity, recent studies of glide trajectories have shown that equilibrium gliding is not the norm for most species. Furthermore, equilibrium theory neglects the aerodynamic differences between species, as well as how a glider can modify its glide path using control. To investigate non-equilibrium glide behavior, we developed a reduced-order model of gliding that accounts for self-similarity in the equations of motion, such that the lift and drag characteristics alone determine the glide trajectory. From analysis of velocity polar diagrams of horizontal and vertical velocity from several gliding species, we find that pitch angle, the angle between the horizontal and chord line, is a control parameter that can be exploited to modulate glide angle and glide speed. Varying pitch results in changing locations of equilibrium glide configurations in the velocity polar diagram that govern passive glide dynamics. Such analyses provide a new mechanism of interspecies comparison and tools to understand experimentally-measured kinematics data and theory. In addition, this analysis suggests that the lift and drag characteristics of aerial and aquatic autonomous gliders can be engineered to passively alter glide trajectories with minimal control effort.

1. Introduction

Animal gliders move horizontally through the air by exchanging potential energy for kinetic energy and by producing and controlling aerodynamic forces [1, 2]. To meet ecologically relevant goals, including predator escape, moving to new foraging locations, searching for mates, or avoiding the forest floor, the glider must control lift and drag forces to dynamically change the glide path and landing location. Glide dynamics have generally been studied using the limited theoretical framework of equilibrium, in which the glide path is straight and performance only depends on a constant lift-to-drag ratio. However, real glide paths are not straight, and lift-to-drag ratio can vary continuously with angle of attack. How animal gliders use their unique morphologies to achieve ecological goals cannot be answered from the equilibrium framework, as it neglects transient dynamics and angle of attack-dependent force coefficients. Furthermore, the evolution of lift-producing wing-like structures, which has occurred over thirty times in arboreal vertebrates [2], suggests that producing and controlling aerodynamic forces is selectively advantageous. To truly understand the gliding behavior of animals, then, suggests that a non-equilibrium framework is required. Here, we conceptualize glide dynamics using lift and drag coefficients that depend on angle of attack and control, which allows the angle of attack to actively vary. These refinements to previous modeling enables a more realistic view of gliding.

The equilibrium gliding assumption states that the resultant aerodynamic force balances the gravitational force. In this condition, the velocity is constant, the glide path is straight and angled down from the horizontal at a constant glide angle, and the glide angle and the lift-to-drag ratio are related by $\cot\gamma = F_L/F_D$ [3]. This assumption has been used to compare gliders and make

predictions of performance. For example, heavier individuals with higher wing loading should glide faster than lighter individuals, but both should have the same equilibrium glide angle [3]. Equilibrium theory also predicts that glide range and energy conversion efficiency will be maximized when the lift-to-drag ratio is maximized [4]. These predictions should be valid for any glider, even though species vary greatly in their size, morphology, and diversity of aerodynamic structures. Examples of this diversity include the dorsoventrally flattened body of gliding snakes [5–9], the inter-limb patagial membrane of gliding mammals [10, 11], the rib-wings of gliding lizards [12, 13], the webbed feet of gliding frogs [14], and body/limbs in wingless hexapods [15, 16] and arachnids [17].

However, there is limited evidence of equilibrium gliding in experimental studies. In one study, 52% of *Draco* glides did not reach equilibrium [13]. In experiments with the flying snake *Chrysopelea paradisi*, only one of 14 glide trials originating from a height of 9.6 m appeared to reach equilibrium [18], and no equilibrium glides were found in eight glide trials beginning from a height of 15 m [5]. Two studies of gliders recorded in the wild found similar results. Body-mounted accelerometers attached to gliding colugos generally indicated greater vertical forces than required for equilibrium [11], and no equilibrium glides were found in long horizontal distance (18 m) glides of northern flying squirrels, *Glaucomys sabrinus*. Simulated glides of *G. sabrinus* required time-varying force coefficients to reproduce the observed trajectories in this species [10]. These studies show that non-equilibrium gliding is dominant in real trajectories.

Observations of non-equilibrium gliding are not unexpected given the coupled effects of animal behavior and aerodynamic force production on glide trajectories. All gliders must accelerate to sufficient velocities to produce appreciable aerodynamic forces, so there is always some non-equilibrium portion at the start of any glide. Similarly, slowing the glide before landing and controlling contact with the substrate requires aerodynamic and postural changes [19]. An animal can also modify force production by changing the wing itself, by varying the camber or aspect ratio with relative limb position [20, 21]. Furthermore, gliders can maneuver volitionally, or make small adjustments to the trajectory to achieve a goal such as landing on a targeted tree [22].

The other source of complexity that can affect glide dynamics is the local airflow interaction with the body. During the ballistic and shallowing phases of gliding that precede equilibrium, the relative air velocity changes continuously in magnitude and in direction. Lift and drag forces scale as the velocity squared, and their lines-of-action depend on the instantaneous flow direction. Additionally, lift and drag coefficients depend strongly on the animal's angle of attack, which changes passively as the glide angle changes, and actively if the animal changes its pitch angle using control. Understanding this coupling of animal behavior and force production requires not only kinematics and force coefficient data, but also modeling to unify experimental observations with physical theory.

Theoretical models have been used to study the effects of force coefficients, wing loading, and initial conditions on glider performance and stability. Models from the late 1800's were developed to understand bird flight [23, 24], but more recent modeling work can be categorized as either particle models or rigid-body models. Particle models consider the glider as a point mass moving in the vertical plane under the influence of lift, drag, and gravity [4, 5, 10, 25]. These models decouple the instantaneous lift and drag coefficients from the glide dynamics, by assuming that the coefficients are either constants or arbitrary functions of time, but not functions of angle of attack. A dominant feature revealed from particle models is damped oscillations in velocity, acceleration, and glide angle time series before the glider reaches equilibrium [4, 5, 24, 25]. Rigid-body models couple both the translational and rotational pitch dynamics of the glider. Jafari *et al* [26] developed two tandem-wing rigid-body models to investigate the passive stability characteristics of flying snakes [26], finding that stable glides are possible, but depend on the initial conditions of pitch and pitch rate. Certain combinations of initial conditions lead to equilibrium glides, whereas other combinations lead to falling with a negligible horizontal velocity.

Here, we used theoretical modeling and a new analysis of the velocity polar diagram (*sensu* Tucker [27]) of horizontal versus vertical velocity to develop a non-equilibrium theoretical framework to understand the mechanics of gliding. This work was specifically motivated by the question, what is the effect of angle-of-attack-dependent lift and drag coefficients on a glider's trajectory dynamics? We developed a rigid-body model using a new rescaling to isolate the effects of the lift and drag coefficients. This rescaling enabled us to test the effect of lift and drag coefficients using simulated glides, with angle-of-attack-dependent force coefficients taken from previous studies. In particular, we used force coefficients from studies of flying squirrels [10, 20], flying snakes [8], sugar gliders [28], flying fish [29], chukar partridge [30] and dragonflies [31]. This broad sampling of animals helps to elucidate commonalities of non-equilibrium gliding, demonstrating the utility of this non-equilibrium framework across phylogenetically diverse species. As future kinematics studies reveal more detailed glide information, this framework can be used to answer questions about how gliders control the trajectory by varying body posture.

2. Methods

We formulate the equations of motion for a glider translating in the vertical x-z plane (figure 1(e)) under the influence of lift, drag, and gravity. We analyze the glider as a rigid body in which angle of attack changes with glide angle and a specified body pitch angle. That is,

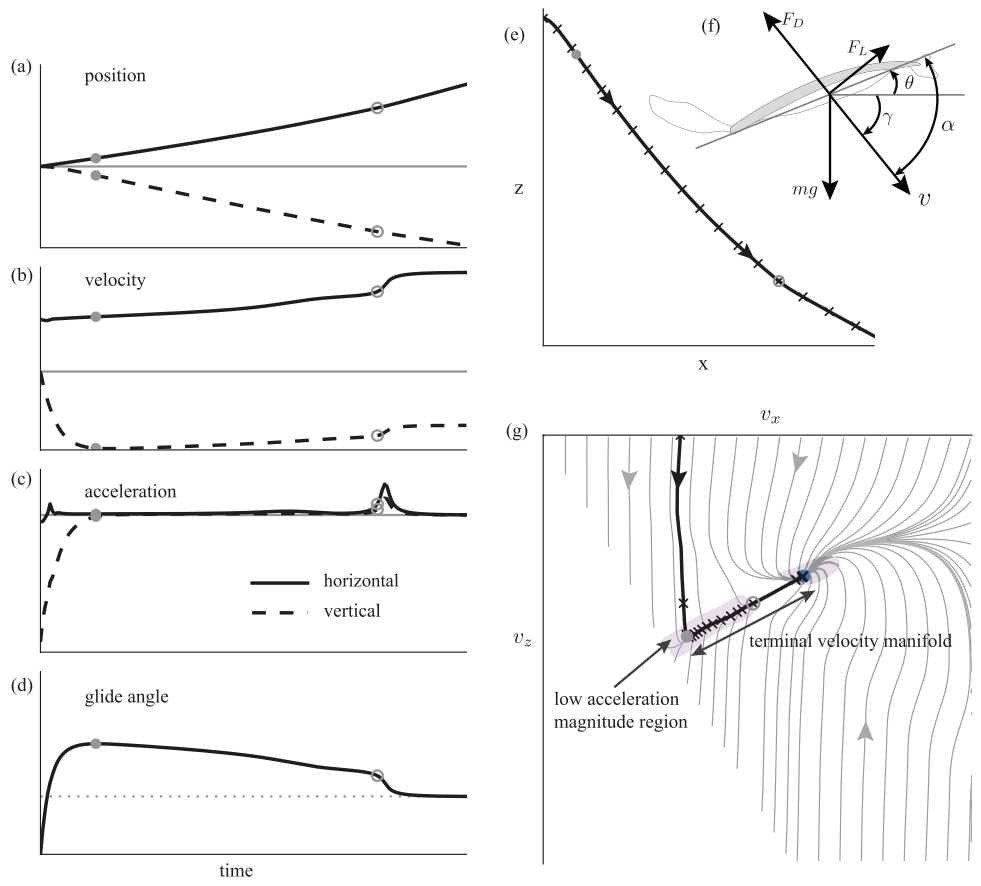

Figure 1. Construction of the velocity polar diagram. (a)–(d) Time histories of position, velocity, acceleration, and glide angle from one simulated glide. The solid circle denotes the location of maximum glide angle, marking the end of the ballistic phase. The open circle denotes an increase in acceleration near the end of the trajectory. The dashed line in (d) indicates the equilibrium glide angle, γ^*. (e) Horizontal (x) and vertical (z) glide path of the simulated glider, where equally spaced points in time are indicated by the 'x' markers, and arrows indicate the direction of forward travel. (f) Schematic of the rigid-body glider model with pitch control analyzed and simulated in this study. (g) Velocity polar diagram, with the simulated trajectory overlaid in black and motion in forward time indicated by the arrow on the trajectory. Gray lines indicate trajectories with different initial conditions of velocity. The end of the ballistic phase occurs when the velocity trajectory transitions onto the terminal velocity manifold. The terminal velocity manifold is surrounded by a low acceleration magnitude region, $\sqrt{a_x^2 + a_z^2} < 0.1\,\mathrm{g}$, indicated by the purple shading. The animal accelerates along the manifold, indicated by loss of shading and denoted with the open circle. The stable equilibrium is denoted by the blue circle; the equilibrium glide angle is the angle subtended between the horizontal axis and a line from the origin to the equilibrium point. The empty wedge-shaped area results from of the angle of attack limitations of the experimentally measured lift and drag coefficients (see supplemental information (stacks.iop.org/BB/12/026013/mmedia)).

we do not write an equation of motion for the rotational dynamics, but instead use the pitch angle to elicit different system responses. To encapsulate a glider's motion in an intuitive and informative manner, we use the velocity polar diagram (figure 1(g)) instead of time series of position, velocity, acceleration, and glide angle (figures 1(a)–(d)). The velocity, acceleration, and glide angle information is embedded in the diagram, and equilibrium gliding can be clearly identified as points where the acceleration vector goes to zero and to which velocity trajectories are attracted to or repelled from.

2.1. Rigid-body model equations of motion

Using the free-body diagram in figure 1(f) for a glider of mass m in an inertial reference frame defined by x and z, we write the equations of motion in the horizontal and vertical directions as

$$\begin{aligned} m\dot{v}_x &= F_\mathrm{L}\sin\gamma - F_\mathrm{D}\cos\gamma \\ m\dot{v}_z &= F_\mathrm{L}\cos\gamma + F_\mathrm{D}\sin\gamma - mg, \end{aligned} \tag{2.1}$$

where the overdot signifies the time derivative, F_L and F_D are the lift and drag forces, v_x and v_z are the velocities in the horizontal and vertical directions, and $a_x = \dot{v}_x$ and $a_z = \dot{v}_z$ are the accelerations in the horizontal and vertical directions. The instantaneous glide angle, $\gamma = -\tan^{-1} v_z/v_x$, is defined as positive for a clockwise rotation from the horizontal axis (i.e. the glide angle will be positive when the animal glides downward). By definition, the drag force acts counter to the local direction of forward travel along the glide trajectory, lift force acts normal to it, and both are written as

$$F_\mathrm{L} = \frac{\rho v^2}{2} S C_\mathrm{L}(\alpha), \quad F_\mathrm{D} = \frac{\rho v^2}{2} S C_\mathrm{D}(\alpha), \tag{2.2}$$

where ρ is air density, $v = \sqrt{v_x^2 + v_z^2}$ is airspeed, S is projected surface area of the glider, $\alpha = \gamma + \theta$ is angle of attack, and θ is pitch angle, which specifies the angle between the mean chord line and the horizontal axis (positive counter-clockwise from the horizontal).

Pitch angle is a free parameter in the model, whereas glide angle is not.

The lift and drag coefficients, $C_L(\alpha)$ and $C_D(\alpha)$, are functions of angle of attack in this model, as determined from lift and drag curves specific to each glider. In general, these curves depend on airfoil shape and Reynolds number [32], and must be determined experimentally. For this analysis, we chose characteristic lift and drag curves for a particular Reynolds number and wing shape, using angle of attack as the only free parameter that determines the instantaneous lift and drag coefficients. Although the lift and drag coefficients are velocity-independent, the lift and drag forces are not. Combining equations (2.1) and (2.2), we arrive at the following expression for the glider's accelerations,

$$\dot{v}_x = \frac{\rho v^2}{2}\frac{S}{m}\left[C_L(\alpha)\sin\gamma - C_D(\alpha)\cos\gamma\right] \quad (2.3)$$

$$\dot{v}_z = \frac{\rho v^2}{2}\frac{S}{m}\left[C_L(\alpha)\cos\gamma + C_D(\alpha)\sin\gamma\right] - g \quad (2.4)$$

2.2. Dimensional analysis

We non-dimensionalize the equations of motion using the chord length c as the characteristic length scale. For a flying snake, the chord length is nominally the flattened aerial width of the animal [5, 8], and for a gliding mammal, it is the distance between the wrist and the ankle along the stretched patagium [21, 33]. The non-dimensional time scale, $T = \sqrt{c/g}$, is found by normalizing by the gravitational acceleration g; it follows that the characteristic velocity scale is $c/T = \sqrt{cg}$. We define the non-dimensional time, velocity, and positions as

$$\bar{t} = \frac{t}{\sqrt{c/g}}, \quad \bar{v} = \frac{v}{\sqrt{cg}}, \quad \bar{p} = \frac{p}{c}.$$

where v is either v_x or v_z and p is either x or z. After substituting the non-dimensional groups into the equations of motion (2.3) and (2.4), we find

$$\frac{d\bar{v}_x}{d\bar{t}} = \epsilon\bar{v}^2\left[C_L(\alpha)\sin\gamma - C_D(\alpha)\cos\gamma\right]$$
$$\frac{d\bar{v}_z}{d\bar{t}} = \epsilon\bar{v}^2\left[C_L(\alpha)\cos\gamma + C_D(\alpha)\sin\gamma\right] - 1$$

where the non-dimensional parameter ϵ can be cast in terms of wing loading, $W_S = mg/S$, as

$$\epsilon = \frac{\rho c}{2}\frac{S}{m} = \frac{\rho g}{2}\frac{c}{W_S}$$

We define ϵ as the universal glide scaling parameter and discuss its significance in section 4.2.

2.3. Rescaling and final equation form

The non-dimensional equations can be further simplified by rescaling velocity and time as $\hat{v} = \sqrt{\epsilon}\,\bar{v}$ and $\hat{t} = \sqrt{\epsilon}\,\bar{t}$. Writing completely in terms of $\hat{v}_x = \hat{v}\cos\gamma$ and $\hat{v}_z = -\hat{v}\sin\gamma$, the Cartesian form of the equations of motion is

$$\hat{v}_x' = -\sqrt{\hat{v}_x^2 + \hat{v}_z^2}\left[C_L(\alpha)\hat{v}_z + C_D(\alpha)\hat{v}_x\right] \quad (2.5)$$

$$\hat{v}_z' = \sqrt{\hat{v}_x^2 + \hat{v}_z^2}\left[C_L(\alpha)\hat{v}_x - C_D(\alpha)\hat{v}_z\right] - 1 \quad (2.6)$$

where prime notation is used as a shorthand for rescaled time derivatives $\frac{d}{d\hat{t}}$. These equations are integrated to construct the velocity polar diagram trajectories. The polar form of the equations, written in terms of the airspeed $\hat{v} = \sqrt{\hat{v}_x^2 + \hat{v}_z^2}$ and glide angle $\gamma = -\tan^{-1}\hat{v}_z/\hat{v}_x$, is

$$\gamma' = -\hat{v}C_L(\alpha) + \frac{\cos\gamma}{\hat{v}} \quad (2.7)$$

$$\hat{v}' = -\hat{v}^2 C_D(\alpha) + \sin\gamma \quad (2.8)$$

Note that the rescaled equations do not depend on body size or wing loading, but only on the lift and drag coefficients. Therefore, any differences in glide performance must result from differences in the lift and drag curves.

2.4. Equilibrium gliding

Equilibrium gliding occurs when the resultant aerodynamic force balances the gravitational force on the glider, producing a constant glide angle and speed. This condition requires that the left-hand sides of expressions (2.5) to (2.8) are zero, resulting in the equilibrium states $(\hat{v}_x^*, \hat{v}_z^*)$ and $(\gamma^*, \hat{v}^*)$. Once the equilibrium glide angle γ^* is known, the equilibrium airspeed $\hat{v}^*$ is determined from equations (2.7) or (2.8), and the equilibrium horizontal and vertical velocities are found using $\hat{v}_x^* = \hat{v}^*\cos\gamma^*$ and $\hat{v}_z^* = -\hat{v}^*\sin\gamma^*$. Simple algebraic manipulation of the equilibrium equations of motion results in the well-known expression for the equilibrium glide angle

$$\frac{F_L}{F_D} = \frac{C_L(\alpha^*)}{C_D(\alpha^*)} = \frac{C_L(\gamma^*+\theta)}{C_D(\gamma^*+\theta)} = \cot\gamma^*, \quad (2.9)$$

where $\alpha^* = \gamma^* + \theta$. This transcendental equation for the equilibrium glide angle γ^* can have multiple solutions, which depend on the number of times the lift-to-drag ratio curve $\frac{C_L}{C_D}$ intersects the $\cot\gamma^*$ curve. Furthermore, the location and number of equilibria depend on the pitch angle θ. Because lift and drag are not analytical expressions of angle of attack, the equilibrium glide angle is found numerically. From equation (2.9), changing the pitch angle shifts the equilibrium glide angle, and to find these values, we consecutively shifted the lift-to-drag ratio curve over a range of specified pitch angles and used the Newton–Raphson root-finding method to locate the intersections. This technique is shown in figure 2, where two equilibrium glide states exist for a pitch of 10° and only one equilibrium for a pitch of −10°.

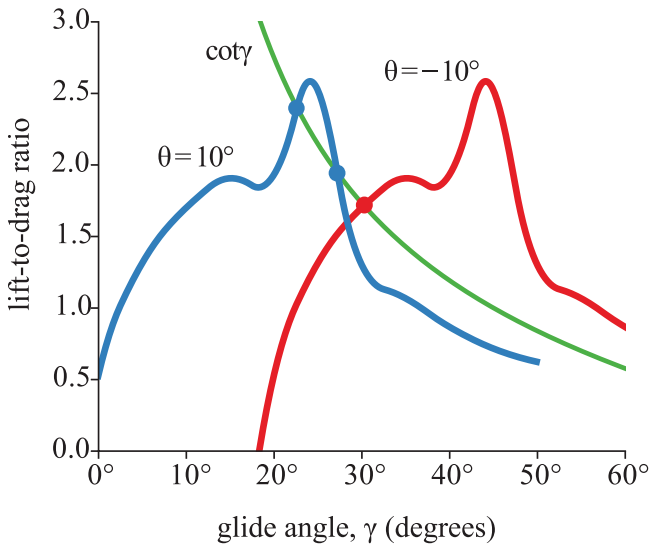

Figure 2. Pitch as a bifurcation parameter. Increasing the body pitch angle θ shifts the lift-to-drag ratio curves horizontally to the left, which changes the number of intersections with cot γ. Each intersection is an equilibrium point, which are indicated by round markers at the intersection points for varying pitch angles. Force coefficient data are for a flying snake cross-sectional shape [8] at Re = 11 000.

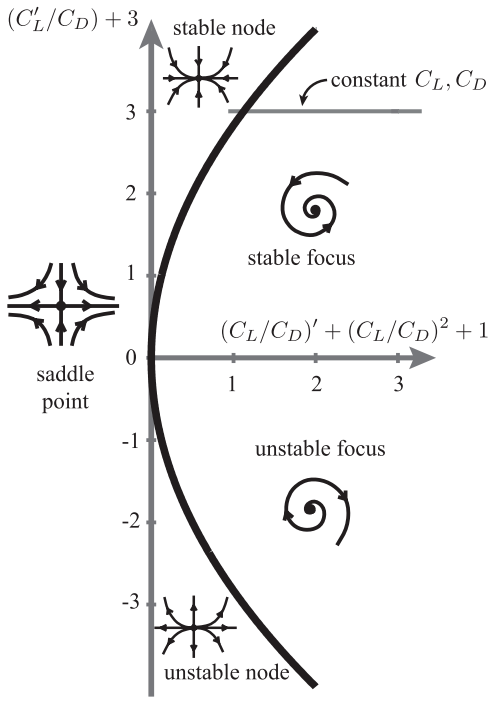

Figure 3. Summary of equilibrium type as a function of lift and drag curves. The equilibrium type is uniquely determined by the lift and drag curves and their slopes evaluated at the equilibrium angle of attack. Previous models of animal gliding, which assumed constant lift and drag coefficients, only observed stable node and stable focus type equilibrium points, as indicated by the horizontal gray line.

2.5. Equilibria type and stability analysis

To determine the stability type and location of equilibrium points in the velocity polar diagram, we use linear stability analysis [34] by classifying the eigenvalues of the Jacobian matrix of partial derivatives for the polar coordinate equations (2.7) and (2.8) evaluated at equilibrium. For this system of two equations, the eigenvalues $\lambda_{1,2}$ are

$$\lambda_{1,2} = \frac{C_D}{2(C_L^2 + C_D^2)^{1/4}}\left(-\tau \pm \sqrt{\tau^2 - 8\Delta}\right), \tag{2.10}$$

$$\tau = \left(\frac{C_L'}{C_D}\right) + 3 \tag{2.11}$$

$$\Delta = \left(\frac{C_L}{C_D}\right)' + \left(\frac{C_L}{C_D}\right)^2 + 1 \tag{2.12}$$

where $\left(\frac{C_L}{C_D}\right)'$ denotes the slope of the lift-to-drag ratio curve. The stability type depends on both the magnitude and slope of the lift and drag curves at equilibrium. This system permits five common types of equilibrium points, based on the signs and magnitudes of τ and Δ: stable and unstable foci, stable and unstable nodes, and saddle points. A summary of these equilibrium types is shown in figure 3.

If lift and drag coefficients are independent of angle of attack, then the primed terms in equations (2.11) and (2.12) are zero, and only stable equilibria are possible. That is, the simulated glider will never have a horizontal velocity of zero and will always reach an equilibrium with some horizontal velocity. Additionally, that equilibrium will be a stable focus if lift-to-drag ratio exceeds the low value of $\frac{1}{2\sqrt{2}} \approx 0.354$ ($\gamma^* > 70.53°$), and otherwise will be a stable node. If lift and drag coefficients are dependent on angle of attack, more dynamical behavior is possible.

2.6. Model input from experimentally measured lift and drag curves

To test the effect of angle-of-attack-dependent force coefficients and the applicability of the non-equilibrium gliding framework, we use aerodynamic coefficient curves (figure 4) from a range of animal gliders, including flying squirrel [20], flying snake [8],

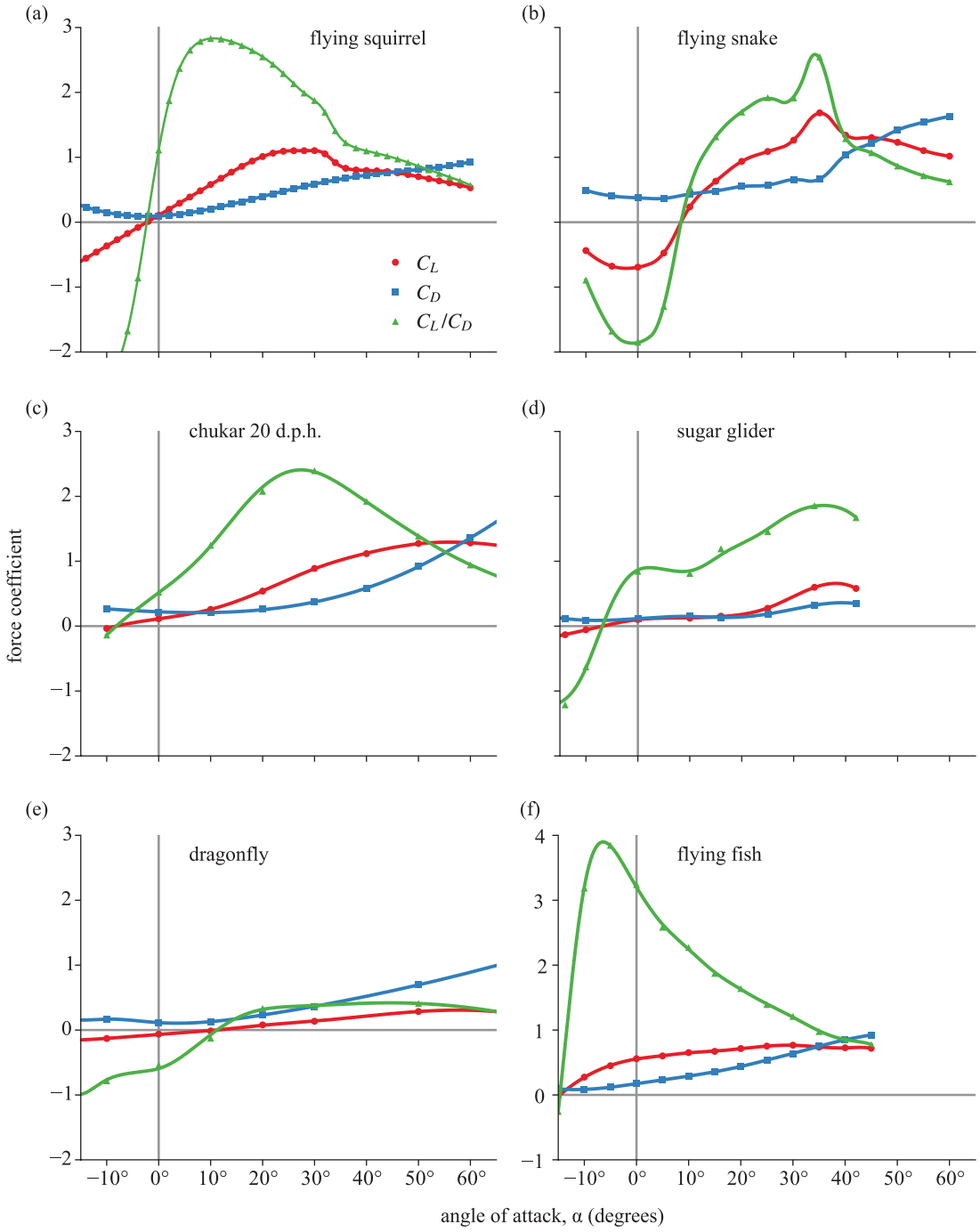

Figure 4. Lift, drag, and lift-to-drag ratio coefficient curves used in this study. Airfoil-based curves for (a) flying squirrels [20], (b) flying snakes [8], and (c) chukar partridge [30], and whole-animal curves for (d) sugar gliders [28], (e) dragonflies [31], and (f) flying fish [29]. Measured values are indicated with markers, and spline-fit values are indicated with solid lines.

sugar glider [28], and flying fish [29], as well as two active flyers, juvenile chukar partridge at 20 days post hatch (d.p.h.) [30], and dragonfly [31]. These species vary in size, Reynolds number, and aerodynamic force-producing structure. The chukar at 20 d.p.h can sustain level flight, but lacks the locomotor capacity of adults, as the wing is still developing and produces only small amounts of lift. Dragonflies use brief periods of gliding, lasting up to 0.5 s and covering 1 m. However, gliding is often interrupted by wingbeats, so glide durations are short (less than 0.2 s, mean of 0.13 s [31]). Coefficient curves are classified in three ways, based on data from previous studies (table 1). The 'airfoil' curves are from wind tunnel experiments of a representative airfoil model. The 'whole animal' curves are from wind tunnel measurements of a deceased and taxidermically-prepared animal. The 'kinematics curves' are reconstructed from recorded glide trials of flying squirrels, and are further discussed below. The coefficient values were smoothed with third-order B-splines to provide a continuous representation for simulations and stability calculations.

Because the aerodynamic coefficients for the entire animal will be different from those of the airfoil alone [35],

Table 1. Types of force coefficient data used in this study. Details describing the derivation of the kinematic squirrel coefficients are presented in the supplemental information.

Animal	Data source	Description	Source
Flying squirrel	Airfoil	Latex membrane in a wind tunnel	[20]
Flying snake	Airfoil	Printed cross-section of *Chrysopelea paradisi* body	[8]
Chukar 20 d.p.h.	Airfoil	Juvenile *Alectoris chukar* wing	[30]
Sugar glider	Whole animal	*Petaurus breviceps papuanus* placed in wind tunnel	[28]
Dragonfly	Whole animal	*Calopteryx splendens* placed in wind tunnel	[31]
Flying fish	whole animal	*Cypselurus hiraii* placed in wind tunnel, model L2	[29]
Kinematic squirrel	Kinematics	Ensemble of *Glaucomys sabrinus* glides	[10]
Individual squirrel	Kinematics	Individual *Glaucomys sabrinus* glides	[10]

we also analyzed force coefficient curves (figure 7(a)) derived from kinematics measurements of flying squirrels gliding to a tree located 18 m from the launch platform [10]. These 'kinematics' coefficient curves were back-calculated from individual glides, as well as from an ensemble of all glides (see supplemental information). To reconstruct the angle-of-attack-dependent coefficients, first the force coefficients were calculated by rearranging equation (2.2). Second, the time-varying angle of attack was approximated as the sum of the calculated glide angle and an assumed pitch angle of zero degrees. We had to approximate the pitch angle because it was not available from the kinematics data. In general, the force coefficient curves measured from wind tunnel tests are of higher quality because (1) the velocities and angles of attack are precisely known, (2) they cover a wider angle of attack range, and (3) noise-magnifying numerical derivatives [36] are not present. Nonetheless, these coefficient curves were included to help synthesize theoretical predictions with observed glides.

2.7. Model assumptions

The complete non-equilibrium glide framework consists of the equations of motion, equations (2.5)–(2.8), and lift and drag coefficients determined from experiments. The model assumes angle-of-attack dependent, but velocity independent, quasi-steady lift and drag coefficients that are representative of the animal mid-glide. Although lift and drag coefficients are velocity independent, the lift and drag forces depend on the instantaneous velocity. Additionally, we do not explicitly model the rotational motion of the glider, but instead treat only one rotational direction, pitch, as a parameter that is systematically varied to elicit different glide performance. Finally, we treat motion in the vertical x-z plane only, ignoring side forces and full three-dimensional glide trajectories resulting from yaw and roll rotations. The above assumptions provide the simplest model to explore the effect of angle-of-attack dependent lift and drag coefficients on a glider's trajectory dynamics.

3. Results

3.1. Structure of the velocity polar diagrams

Velocity polar diagrams for the airfoil and whole-animal-based lift and drag curves are shown in figure 5 for two different pitch angles. In these plots, initial conditions from the animal gliders originate near the origin of the diagram, with a near-zero vertical velocity and low horizontal velocity. These plots show that only certain equilibrium glides can be reached for the initial conditions typically observed in real glides. The velocity polar diagrams generally have multiple equilibria including stable nodes and saddle points. The stable and unstable manifolds of the saddle point delineate the basins of stability of stable glides. The upper stable branch of the saddle point, which runs vertically through the diagrams, acts as a separatrix (*sensu* Strogatz [34]) and can block accessibility to low glide angle equilibrium points. Additionally, saddles show that there are stable and unstable directions in the velocity polar diagram; these directions determine the glider's trend toward equilibrium.

Nearly all velocity trajectories in figure 5 (except for figure 5(dii)) fall quickly onto a one-dimensional manifold. If the trajectory originates in the basin of stability of the equilibrium point, the trajectory moves along the manifold and stable gliding is achieved. Otherwise, the trajectory is pushed to a steep glide where the horizontal velocity is low and the animal is in effect falling. The initial quick descent of the glider to the manifold corresponds to the ballistic phase of gliding (figures 1(d) and (g)), and movement along the manifold corresponds to the shallowing phase of gliding. We designate this one-dimensional manifold as the 'terminal velocity manifold' as it is a higher-dimensional analog of the terminal velocity, and dynamics along it are a relatively slow evolution toward stable equilibrium. The terminal velocity manifold is approximated by the curve of zero vertical acceleration, the v_z nullcline, along which equation (2.6) is zero. A trajectory in the vicinity of the nullcline would be in a near-vertical force balance, with the vertical component of the total aerodynamic force balancing the weight of the gliders. Nullclines are shown on the flying snake and chukar velocity polar diagrams (figures 5(bi), (ci), and (cii)). These curves pass through any equilibrium points present in the velocity polar diagram, and best approximate the terminal velocity manifold locally around the stable node. If a saddle point exists (e.g. figures 5(ai), (aii), (bii), (cii), and (fi)), then the terminal velocity manifold is also approximated by the unstable branch of a saddle point and the less-stable manifold of a stable node. Furthermore, we can

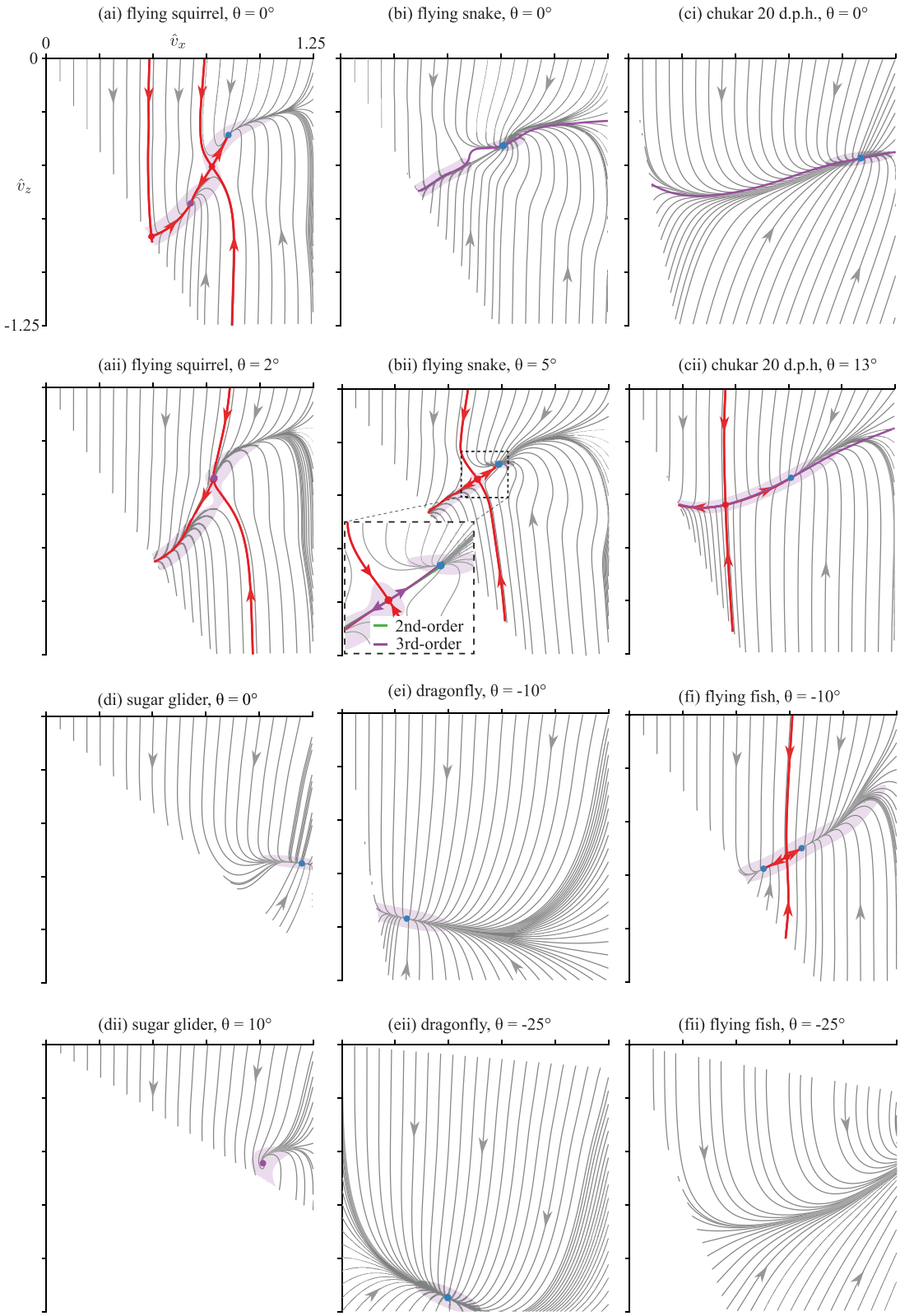

Figure 5. Velocity polar diagrams. Two different pitch values, indicated by (i) and (ii), are shown for (a) flying squirrels, (b) flying snakes, (c) chukar partridge, (d) sugar gliders, (e) dragonflies, and (f) flying fish. Pitch values are specified by vertical lines in figure 6. Gray lines are simulated glide trajectories, and arrows indicate motion along the trajectory through time. Equilibrium gliding is indicated by circle markers, and the glide angle is read as the angle subtended from the horizontal axis as before to the equilibrium point(s). Saddle points and their stable and unstable branches are indicated in red, with separatrices running vertically to the saddle points. The inset in (bii) shows 2nd and 3rd-order accurate analytical approximations of the terminal velocity manifold in the vicinity of the saddle point equilibrium. Vertical velocity nullclines, where the vertical acceleration is zero, are shown in (bi), (ci), and (cii), as the solid purple line passing though the equilibrium points and near the terminal velocity manifold. (ai) Flying squirrel, $\theta = 0$. (aii) Flying squirrel, $\theta = 2$. (bi) Flying snake, $\theta = 0$. (bii) Flying snake, $\theta = 5$. (ci) Chukar 20 d.p.h., $\theta = 0$. (cii) Chukar 20 d.p.h., $\theta = 13$. (di) Sugar glider, $\theta = 0$. (dii) Sugar glider, $\theta = 10$. (ei) Dragonfly, $\theta = -10$. (eii) Dragonfly, $\theta = -25$. (fi) Flying fish, $\theta = -10$. (fii) Flying fish, $\theta = -25$.

approximate the terminal velocity manifold analytically (see Supplemental Information), as shown in the inset of figure 5(bii).

Low-acceleration regions ($a \leqslant 0.1\,g$ where $a = \sqrt{a_x^2 + a_z^2}$) are identified by shading in all velocity polar diagrams in figure 5. These regions are located around the equilibrium points and along terminal velocity manifolds, which indicates that the glider will exhibit little change in velocity while far from equilibrium, with glide dynamics dictated by the direction of the manifold. Trajectories can also leave the low-acceleration region (figures 5(bi) and (bii)) while moving along the terminal velocity manifold towards equilibrium. In these velocity polar diagrams, this results from the peak in the lift-to-drag ratio of the flying snake coefficients near an angle of attack 35° (figure 4(b)).

3.2. Pitch bifurcation diagrams

The equilibrium points and corresponding equilibrium glide angles shown in figure 5 are summarized in a single bifurcation diagram for each glider in figure 6. For a given pitch angle, these diagrams show the stability type and glide angle of all possible equilibrium glides.

The bifurcation diagrams show multiple co-existing equilibrium points at high and low angles of attack, which persist over a range of pitch angles. The flying squirrel bifurcation diagram (figure 6(a)) shows that upwards of four co-existing equilibrium points are possible. In general, only a single stable equilibrium exists when pitch is negative, with equilibrium glide angles relatively insensitive to pitch. We refer to the slope of the pitch bifurcation curve along the branch of stable equilibrium points as the 'pitch sensitivity', calculated as $\mathrm{d}\gamma^*/\mathrm{d}\theta$. For the flying squirrel bifurcation diagram, a saddle-node bifurcation occurs at a maximum pitch of 2°. Beyond this pitch angle, no shallow equilibrium glides are observed, and the glider is essentially falling. The flying snake bifurcation diagram (figure 6(b)) is similar to the flying squirrel bifurcation diagram, except that more than four equilibria are possible at select pitch angles around 1°. The stable node and saddle point are much closer, and no equilibrium glides are found beyond the saddle-node bifurcation at a pitch angle of 12°.

The chukar, sugar glider, and dragonfly bifurcation diagrams (figures 6(c)–(e)) show a flat equilibrium glide angle region over a large range of pitch angles. Due to the low lift-to-drag ratio of the dragonfly, equilibrium glides are steep, being nominally 70° in glide angle. The flying fish and dragonfly bifurcation diagrams show that only negative pitch angles allow stable equilibria; in this condition, a flying fish or dragonfly would be nose-down at equilibrium.

3.3. Velocity polar diagrams from kinematics data

To demonstrate how these analytical methods can be applied to experimental data, we used mean force coefficients from a flying squirrel glide experiment (figure 7(a)) as model inputs to construct both a bifurcation diagram (figure 7(b)) and velocity polar diagrams at zero and positive pitch values (figures 7(ci) and (cii)). The kinematic squirrel velocity trajectories show spiraling behaviors around both stable or unstable foci. This spiraling is also present in the velocity polar diagrams derived from individual glide trials (figures 7(d) and (e)), with the experimental velocity trajectory overlaid.

The kinematic squirrel bifurcation diagram (figure 7(b)) shows foci at low equilibrium glide angles that are insensitive to pitch; in particular, the equilibrium glide angle is almost constant from −5 to 4°. The two solid lines in this figure indicate the maximum and minimum glide angles of an unstable periodic orbit, which exists between Hopf bifurcation points at $\theta \approx -1°$ and $\theta \approx 5.6°$. This corresponds to the unstable periodic orbit in figure 7(ci) and the only closed contour in the velocity polar diagram. This Hopf bifurcation occurs any time the equilibrium changes from an unstable to a stable focus (and vice versa), and the characteristics of the resulting periodic orbit can be computed analytically given the lift and drag curves (see supplemental information).

4. Discussion

We have developed a dynamical systems framework to understand non-equilibrium animal gliding based only on the lift and drag coefficients. In this conceptualization of gliding, equilibrium is represented as a point in the velocity polar diagram where the accelerations are zero; trajectories will progress towards or away from equilibrium depending on the initial conditions and the equilibrium type. Analysis of the velocity polar diagram indicates that pitch angle has a large effect on the glide trajectory and that animal gliding has more complicated dynamics than previously realized. However, these dynamics can be systematically explored using the velocity polar diagram and by incorporating the lift and drag coefficient curves into the equation of motion.

4.1. Effect of lift and drag coefficients

Because lift and drag coefficients are the only model inputs, the analysis presented here can be viewed as a parametric study of representative lift and drag curves and how the structure of these curves affects non-equilibrium gliding. The analytically-derived expressions for equilibrium type (figure 3) and the general topology of the velocity polar diagrams (figure 5) indicate commonalities in how glide trajectories proceed based solely on the lift and drag curves. First, multiple equilibria are possible, and these generally occur for slightly negative to positive pitch values. Second, unstable equilibria are possible, particularly saddle points which appear along a terminal velocity manifold. Third, spiraling motion in the velocity polar

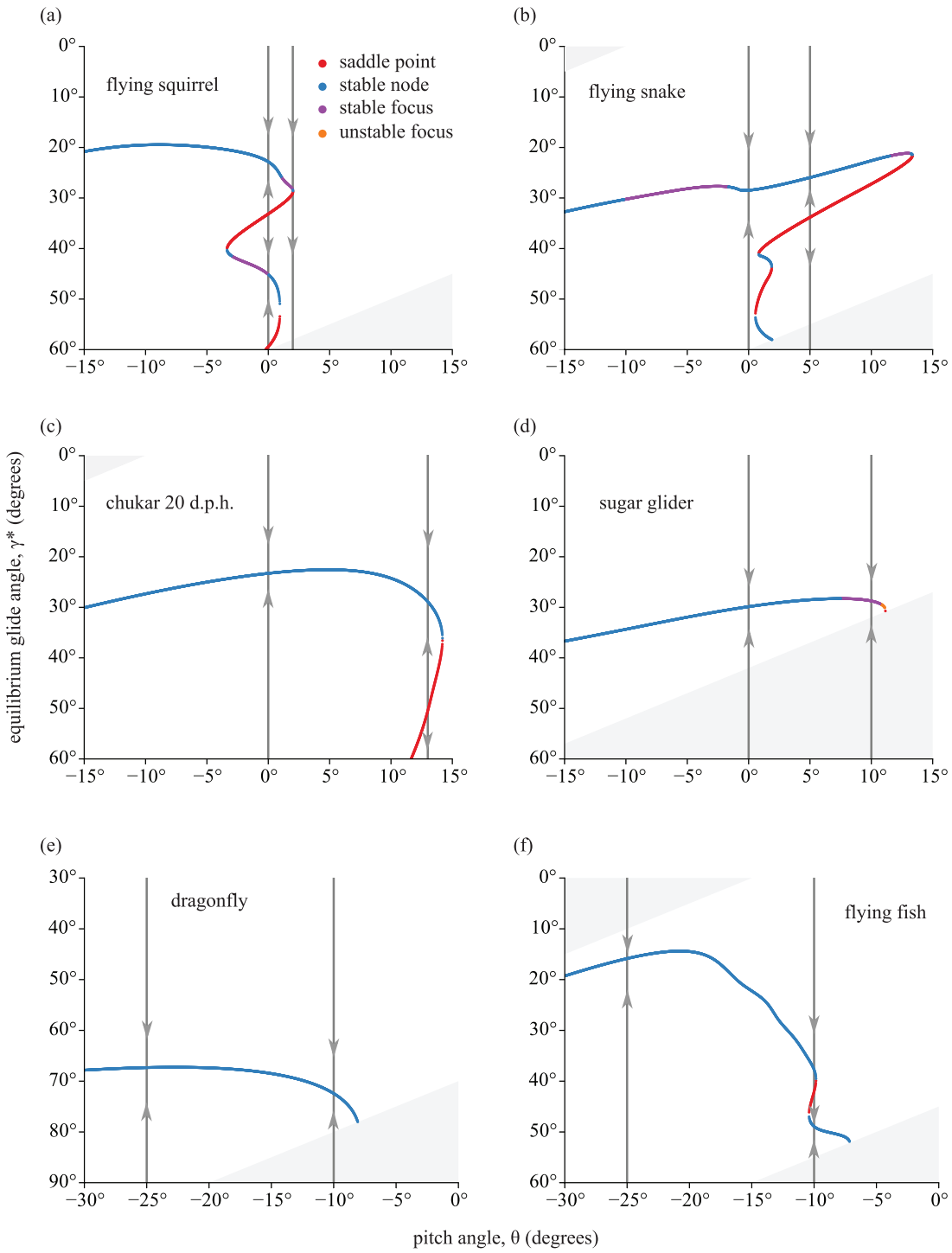

Figure 6. Pitch bifurcation diagrams for equilibrium glide angle γ^* as pitch angle θ varies. Diagrams correspond to (a) flying squirrels, (b) flying snakes, (c) chukar partridge, (d) sugar gliders, (e) dragonflies, and (f) flying fish. Equilibrium glide angles are found as intersection(s) of the bifurcation curve with vertical lines at a specified pitch angle, with multiple intersections indicating multiple equilibrium points. Colors correspond to different equilibrium types; cool colors are locally attracting and warm colors are locally repelling. Vertical lines indicate pitch angles used in the velocity polar diagrams in figure 5, and the arrows on these lines indicate the passive direction change of glide angle. Not all angles of attack were available in the original data; these regions are indicated with gray shading.

diagram is seen in several of the diagrams, particularly from the kinematics curves, but also when lift and drag coefficients are constants.

The difference in velocity polar diagram structure when there is a terminal manifold or when there is a focus-type equilibrium suggests future extensions of this work to investigate if gliders switch between different glide motifs. The motion around a focus-type equilibrium in the kinematics-based flying squirrel velocity polar diagrams (figures 7(c)–(e)), with a decrease in vertical velocity throughout the trajectory, is not seen in the airfoil-based velocity polar diagrams (figure 5). These different gliding motifs could provide complementary means to modify the glide path, but

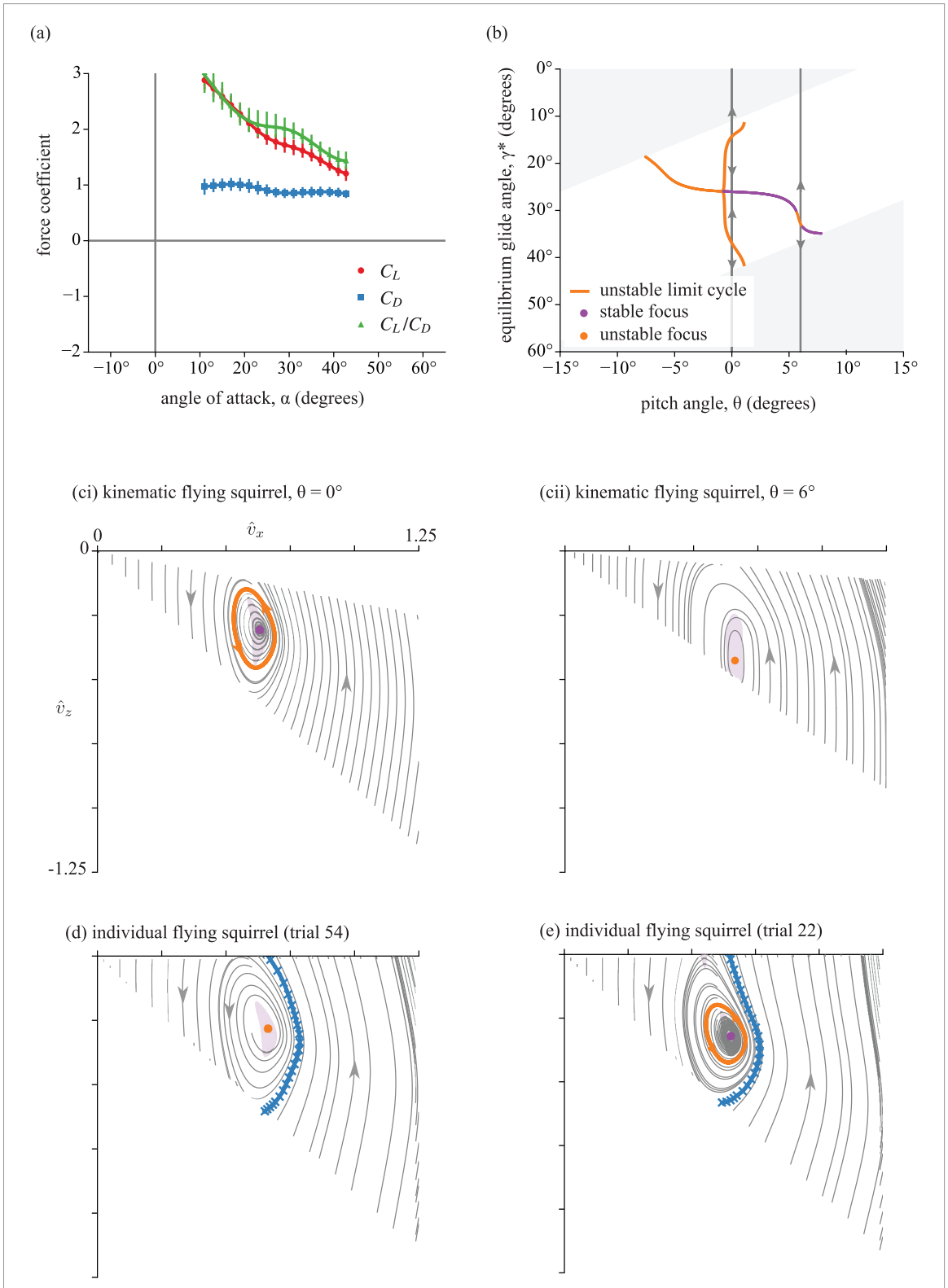

Figure 7. Non-equilibrium glide framework applied to kinematics data of flying squirrels from [10]. (a) Aerodynamic coefficients derived from an ensemble of kinematics measurements. Solid points are mean ± s.e.m. (b) Pitch bifurcation diagram. ((ci) and (cii)) Velocity polar diagrams at zero and positive pitch angles, respectively. The closed contour in (ci) is a periodic orbit due to a Hopf bifurcation. ((d) and (e)) Velocity polar diagrams derived from individual glide trials. The calculated velocity trajectory is indicated in blue and equal time points are indicated at 0.08 s intervals. Note that all velocity polar diagrams have the same limits because the kinematics data have been non-dimensionalized and rescaled. (a) angle of attack, α(degrees). (b) pitch angle, θ(degrees). (ci) kinematic flyimg squirrel, $\theta = 0°$. (cii) kinematic flyimg squirrel, $\theta = 6°$. (d) individual flying squirrel (trial 54). (e) individual flying squirrel (trial 22).

how the animal switches between them is unknown. For example, the focus-based motif should lessen landing forces, because the vertical velocity is near zero or merely slightly positive at the end of the glide. However, the animal would have higher accelerations throughout the glide, which in theory would require more control

authority to maintain stability. In the terminal velocity manifold motif, accelerations are lower for the majority of the glide, but a large pitch-up maneuver would be required for landing to lower the airspeed. How the animal switches between these motifs with changes to lift and drag coefficients, or with unsteady aerodynamic and/or fluid-structure interaction effects [37–39], are important considerations for future work.

Calculating the kinematics-based lift and drag coefficient curves was done as a way to compare measured animal trajectories to model predictions. The velocity polar diagrams derived from wind tunnel measurements (figures 5(ai), (aii), (di), and (dii)) are substantially different from the kinematics-based ones (figures 7(c)–(e)). There are several possible reasons for this. One possibility is that the kinematics data are insufficient (due to undersampling, noise, or experimental error) to derive force coefficient curves. The kinematics data lack the ballistic phase of the glide, and the assumption of zero pitch angle used to derive the kinematics-based curves is likely to be invalid over part of the glide. Another possibility is that wind tunnel coefficient curves do not accurately represent the whole-animal aerodynamics in flight. This is most likely true for the artificial membrane curves, in which a thin latex sheet represents the patagial membrane, but does not include the limbs and tail of the flying squirrel. The sugar glider coefficient curves provide an intermediary to understand whole-animal lift and drag characteristics, as it is of a taxidermically prepared mammal in a likely flight configuration. In fact, these curves show spiraling in the velocity polar diagram (figure 5(dii)) for certain positive pitch angles, which is a likely flight posture used by flying squirrels [19]. Spiraling is also seen in the kinematics-based velocity polar diagrams in figures 7(c)–(e).

4.2. Comparison to other modeling studies of gliding

In the model presented here, the magnitude and orientation of the aerodynamic force vectors are modulated by pitch angle. Previous particle models were not directional, with the aerodynamic force vectors evolving under passive dynamics only [4, 5, 10, 25]. However, both types of models neglect rotational stability and consider translational motion assuming quasi-steady aerodynamics.

A significant difference between previous models and the model presented here is that lift and drag coefficients are not constants, but instead are angle of attack dependent. This difference results in drastically different simulated glide trajectories in both position and velocity space. When lift and drag coefficients are constants, only stable equilibria are possible, meaning that there are no physically realistic values of initial velocity or wing loading that result in falling directly downward. Additionally, these equilibria are predominantly of the focus type—the oscillatory behavior observed in previous models was a consequence of the lift-to-drag ratio only. This oscillatory behavior is very evident when viewed in the velocity polar diagram (see figure 1 in the supplemental information). The glider does not smoothly transition from the ballistic phase to motion along the terminal velocity manifold, but instead oscillates towards an equilibrium glide.

When aerodynamic force coefficients depend on angle of attack, coexisting stable and unstable equilibrium points are possible. These equilibrium points organize the global topology of the velocity polar diagram and segregate regions that are reachable from typically low takeoff velocities, rendering certain stable glide trajectories infeasible. Certain equilibria become inaccessible when a saddle point appears along the terminal velocity manifold. Because glides originate in the upper left quadrant of the velocity polar diagram, with near-zero vertical velocity and small horizontal velocity, the upper branch of the saddle point's stable manifold acts as a separatrix, which blocks low glide angle equilibrium points. The appearance of a saddle point explains the basin of stability observations in the $\theta_0 - \dot{\theta}_0$ space in previous snake modeling work [26], as certain initial condition combinations can lead to unsuccessful glides. In that previous study, the pitch rate affects the traversal of the non-autonomous velocity space, where this separatrix appears and blocks stable glides. This effect can also be understood as sweeping through pitch angle in the pitch bifurcation diagram in figure 6(b), where moving from negative to slightly positive pitch leads to a saddle-node bifurcation.

The newly presented non-dimensionalization and rescaling of the equations of motion is a significant difference from previous studies. This rescaling reduces the difference between species to their lift and drag coefficient curves only. The universal glide scaling parameter ($\epsilon \propto c/W_S$) not only facilitates modeling and normalization of experimental trajectories, but provides a metric to compare gliders based on their chord length and wing loading. Under geometric scaling of isometry, and assuming $c \propto L$ and $m \propto L^3$, one would expect chord length to scale as $c \propto m^{1/3}$. Experimental data suggest that wing loading scales isometrically, $W_S \propto m^{1/3}$ [1], so one would therefore expect $\epsilon =$ constant for a given species. The universal glide scaling parameter is shown in figure 8 for a variety of animal gliders across several orders of magnitude of mass. The scaling of ϵ with mass is not as evident as with wing loading [1], but there appear to be three distinct groupings. The first grouping has an ϵ value of 0.1 and includes dragonflies only. The next grouping has an ϵ of 0.04 and includes *Draco*, squid, and mammals. The third grouping, with an ϵ of 0.003, includes flying snakes and flying fish. For flying snakes, ϵ is nearly constant over two orders of magnitude in mass, and for *Draco*, ϵ is nearly constant over one order of magnitude in mass. These different scaling groups suggest that the chord length used to non-dimensionalize the equations of motion has a large effect on ϵ for different gliding species.

The universal glide scaling parameter also helps to explain why smaller individuals with lower wing loading are generally better gliders, covering more

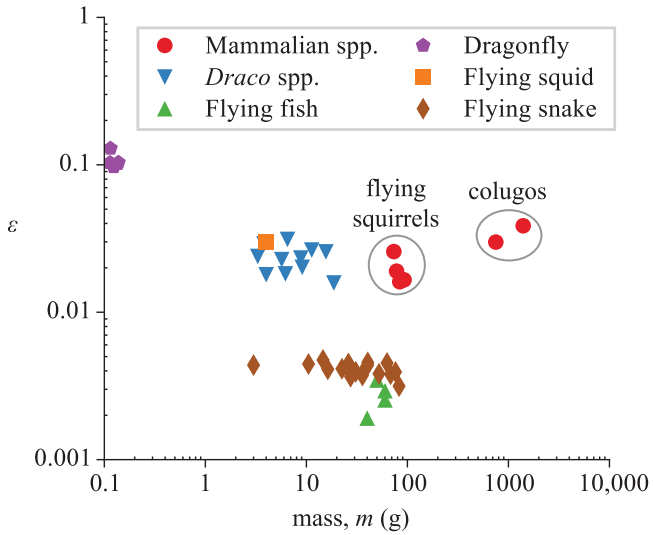

Figure 8. Universal glide scaling parameter ϵ for gliding animals. Mammalian data for flying squirrels, sugar gliders, and colugos are from [10, 11, 21, 33, 40], *Draco* data are from [12, 13], flying fish (*Cypselurus hiraii*) data are from [29], dragonfly (*Sympetrum sanguine*) data are from [31], flying squid (*Sthenoteuthis ptrepus*) data are from [1, 41], and flying snake (*Chrysopelea paradisi*) data are from [1, 18, 42].

horizontal distance from a given take-off height. The framework presented here identifies equilibrium points in the velocity polar diagram, but it does not specify the time required to reach equilibrium. By converting both time and velocity back to physical units using ϵ,

$$t = \sqrt{\frac{2W_S}{\rho g^2}}\,\hat{t}, \qquad v = \sqrt{\frac{2W_S}{\rho}}\,\hat{v} \tag{4.1}$$

we see that both dimensional time and velocity are proportional to the square root of wing loading. Because the time to equilibrium $\hat{t}$ is fixed in (4.1), the glider with lower wing loading will reach equilibrium sooner. If a large and a small individual were to take off from the same physical height and with the same initial conditions in the velocity polar diagram, the smaller individual would traverse more of the velocity space before landing. This would correspond with a higher shallowing rate, lower velocity, and greater horizontal distance traveled.

4.3. Implications for animals that glide

The global view of gliding developed here provides insight into how a glider's translational motion changes with pitch. The results of this work show that once the glider is at equilibrium, changing pitch angle has only a small effect on glide angle. For example, for the sugar glider (figure 6(d)), the equilibrium glide angles change only 10° over a pitch range of 25°. A similar trend holds for the other wind-tunnel based bifurcation diagrams, in which the low glide angle equilibrium is relatively insensitive to pitch. The initial launch parameters and the ballistic glide phase are therefore important because they determine how close to the basin of stability the glider is, and if control is needed to select a stable equilibrium. This analysis suggests that animals could select pitch values to avoid unstable features in the velocity polar diagram, with a worst-case scenario resulting in a fall with negligible horizontal velocity. A negative pitch angle shortly after launch and through the ballistic phase will confer greater translational stability, and will also act to direct the lift vector horizontally.

Additionally, hysteresis effects are possible as the pitch angle changes. The equilibrium glide angle can increase rapidly if the pitch angle increases above a critical threshold (figures 6(a) and (b)). To re-establish a low glide angle equilibrium glide, a glider would have to decrease its pitch to a negative value so that only the upper stable branch of equilibria are possible. Therefore, a pitch-up maneuver prior to landing would not only slow the animal, but may remove all equilibria from the velocity polar diagram, so the animal would begin to fall. Only very steep glides are possible for some animals, such as dragonflies (figure 6(e)) and gliding arthropods. Arthropod glide trajectories consist of large glide angles between 70°–75° and small lift-to-drag ratio of approximately 0.3 [15–17]. Although lift and drag coefficient data are not available, these steep trajectories suggest velocity polar diagram structure similar to figure 5(e), with steep glides to a stable equilibrium.

The framework presented here also helps to address the question of if and when equilibrium is reached in gliding, as it clearly distinguishes true equilibrium where accelerations are zero, from equilibrium-like gliding in the shallowing phase and along the terminal velocity manifold where accelerations are small. Measured fluctuations of the glide path, which indicate non-equilibrium gliding, can occur for several reasons. One possibility is the animal in such a trajectory is using small postural changes to maintain a particular pitch angle or to slightly alter the glide path. Another possibility is that experimental errors, from digitization and numerical derivatives of position data, give the appear-

ance of spurious fluctuations. In either case, although its velocities and accelerations are changing, the glider is in effect confined to a region around equilibrium as it moves along the v_z nullcline and the terminal velocity manifold. The animal's trajectory in the velocity polar diagram, or its pitch angle history when viewing the pitch bifurcation diagram, can then be used to quantify the amount of non-equilibrium gliding and possibly control effort to maintain stability.

Lastly, the non-equilibrium gliding framework helps to elucidate the role of aerodynamic coefficients and airfoil performance on the evolution of flight. It has been previously suggested that phugoid gliding (long-wavelength oscillation of the glide trajectory) was used by the feathered dinosaur *Microraptor gui* [43]. These phugoid oscillations can be viewed as the position-space representation of a stable focus in the velocity polar diagram. Other phase-space structures, such as the terminal velocity manifold and the acceleration along it, likely confer other stability or energetic advantages. Detailed wind tunnel measurements of aerodynamic coefficients of *Microraptor gui* [44] can be used in the framework presented here to quantify how phase-space structures lead to variable glide performance between prehistoric and modern gliders.

5. Conclusions

We have presented a non-equilibrium framework of animal gliding based on the underlying structure in the equations of motion and empirically measured lift and drag coefficient curves. We find several structures in the velocity polar diagram relevant to gliders, including a terminal velocity manifold surrounded by low acceleration magnitude regions, saddle points that define the basin of stability of low glide angle equilibrium points, and equilibrium points of varying type and stability that affect glide performance. This framework not only clarifies previous modeling studies which assumed constant lift-to-drag ratio, but indicates how an animal can actively control its glide trajectory using pitch angle. New pitch bifurcation diagrams show how the equilibrium points change with pitch angle, and how the equilibrium points alter the structure of the velocity polar diagram during all phases of gliding. As more detailed kinematics data become available, this framework can be used to understand how experimentally recorded gliders alter their trajectory through control of body orientation and the likely drivers of this control. This framework also suggests that the glide dynamics of engineered aerial and aquatic autonomous gliders can be designed to exploit the structure of the velocity polar diagram. To exploit the structure of the velocity polar diagram would require designing angle-of-attack dependent lift and drag coefficients such that equilibria of known type, stability, and equilibrium glide angle are placed in the velocity polar diagram. The autonomous glider would then only need small actuations in pitch angle to passively switch to different glide states.

Acknowledgments

We thank Gary Nave for comments and critical reading of early versions of the manuscript. This work was partially supported by the National Science Foundation under grants 1351322 to JJS, 1150456 to SDR, and grant 0966125 to SDR and JJS. This work was conducted in partial fulfillment of dissertation requirements for IJY.

References

[1] Socha J J, Jafari F, Munk Y and Byrnes G 2015 How animals glide: from trajectory to morphology *Can. J. Zool.* **93** 901–24
[2] Dudley R, Byrnes G, Yanoviak S P, Borrell B, Brown R M and McGuire J A 2007 Gliding and the functional origins of flight: biomechanical novelty or necessity? *Annu. Rev. Ecol. Evol. Systematics* **38** 179–201
[3] Vogel S 2009 *Glimpses of Creatures in Their Physical Worlds* (Princeton, NJ: Princeton University Press)
[4] Willis D, Bahlman J, Breuer K and Swartz S 2011 Energetically optimal short-range gliding trajectories for gliding animals *AIAA J.* **49** 2650–7
[5] Socha J J, Miklasz K, Jafari F and Vlachos P P 2010 Non-equilibrium trajectory dynamics and the kinematics of gliding in a flying snake *Bioinspiration Biomimetics* **5** 045002
[6] Socha J J 2011 Gliding flight in *Chrysopelea*: turning a snake into a wing *Integr. Comparative Biol.* **51** 969–82
[7] Miklasz K, LaBarbera M, Chen X and Socha J J 2010 Effects of body cross-sectional shape on flying snake aerodynamics *Exp. Mech.* **50** 1335–48
[8] Holden D, Socha J J, Cardwell N D and Vlachos P P 2014 Aerodynamics of the flying snake *Chrysopelea paradisi*: how a bluff body cross-sectional shape contributes to gliding performance *J. Exp. Biol.* **217** 382–94
[9] Krishnan A, Socha J J, Vlachos P P and Barba L A 2014 Lift and wakes of flying snakes *Phys. Fluids* **26** 031901
[10] Bahlman J W, Swartz S M, Riskin D K and Breuer K S 2013 Glide performance and aerodynamics of non-equilibrium glides in northern flying squirrels (*Glaucomys sabrinus*) *J. R. Soc. Interface* **10** 20120794
[11] Byrnes G, Lim N T-L and Spence A J 2008 Take-off and landing kinetics of a free-ranging gliding mammal, the Malayan colugo (*Galeopterus variegatus*) *Proc. R. Soc.* B **275** 1007–13
[12] McGuire J A 2003 Allometric prediction of locomotor performance: an example from southeast Asian flying lizards *Am. Nat.* **161** 337–49
[13] McGuire J A and Dudley R 2005 The cost of living large: comparative gliding performance in flying lizards (Agamidae: *Draco*) *Am. Nat.* **166** 93–106
[14] McCay M G 2001 Aerodynamic stability and maneuverability of the gliding frog *Polypedates dennysi J. Exp. Biol.* **204** 2817–26
[15] Yanoviak S P, Dudley R and Kaspari M 2005 Directed aerial descent in canopy ants *Nature* **433** 624–6
[16] Munk Y, Yanoviak S P, Koehl M A R and Dudley R 2015 The descent of ant: field-measured performance of gliding ants *J. Exp. Biol.* **218** 1393–401
[17] Yanoviak S P, Munk Y and Dudley R 2015 Arachnid aloft: directed aerial descent in neotropical canopy spiders *J. R. Soc. Interface* **12** 20150534
[18] Socha J J, O'Dempsey T and LaBarbera M 2005 A 3D kinematic analysis of gliding in a flying snake, *Chrysopelea paradisi J. Exp. Biol.* **208** 1817–33
[19] Paskins K E, Bowyer A, Megill W M and Scheibe J S 2007 Take-off and landing forces and the evolution of controlled gliding

in northern flying squirrels *Glaucomys sabrinus J. Exp. Biol.* **210** 1413–23
[20] Song A, Tian X, Israeli E, Galvao R, Bishop K, Swartz S and Breuer K 2008 Aeromechanics of membrane wings with implications for animal flight *AIAA J.* **46** 2096–106
[21] Bishop K L 2006 The relationship between 3D kinematics and gliding performance in the southern flying squirrel, *Glaucomys volans J. Exp. Biol.* **209** 689–701
[22] Vernes K 2001 Gliding performance of the Northern flying squirrel (*Glaucomys sabrinus*) in mature mixed forest of Eastern Canada *J. Mammal.* **82** 1026–33
[23] Zhukovskii N Y 1891 On soaring of birds *Tr. Otd. Fiz. Nauk Obs. lyubit. yestestvz.* **4** 2
[24] Andronov A A, Vitt A A and Khaikin S E 1966 *Theory of Oscillators* (Reading, MA: Addison-Wesley)
[25] Dyke G, de Kat R, Palmer C, van der Kindere J, Naish D and Ganapathisubramani B 2013 Aerodynamic performance of the feathered dinosaur *Microraptor* and the evolution of feathered flight *Nat. Commun.* **4** 2489
[26] Jafari F, Ross S D, Vlachos P P and Socha J J 2014 A theoretical analysis of pitch stability during gliding in flying snakes *Bioinspiration Biomimetics* **9** 025014
[27] Tucker V A 1998 Gliding flight: speed and acceleration of ideal falcons during diving and pull out *J. Exp. Biol.* **201** 403–14
[28] Nachtigall W, Grosch R and Schultze-Westrum T 1974 Gleitflug des Flugbeutlers *Petaurus breviceps papuanus* (Thomas) I *J. Comparative Physiol.* **92** 105–15
[29] Park H and Choi H 2010 Aerodynamic characteristics of flying fish in gliding flight *J. Exp. Biol.* **213** 3269–79
[30] Heers A M, Tobalske B W and Dial K P 2011 Ontogeny of lift and drag production in ground birds *J. Exp. Biol.* **214** 717–25
[31] Wakeling J M and Ellington C P 1997 Dragonfly flight I. Gliding flight and steady-state aerodynamic forces *J. Exp. Biol.* **200** 543–56
[32] Sunada S, Sakaguchi A and Kawachi K 1997 Airfoil section characteristics at a low Reynolds number *J. Fluids Eng.* **119** 129–35
[33] Bishop K L 2007 Aerodynamic force generation, performance and control of body orientation during gliding in sugar gliders (*Petaurus breviceps*) *J. Exp. Biol.* **210** 2593–606
[34] Strogatz S H 2001 *Nonlinear Dynamics and Chaos: with Applications to Physics, Biology, Chemistry, and Engineering* (Boulder, CO: Perseus Books)
[35] Milne-Thomson L M 1966 *Theoretical Aerodynamics* (New York: Dover)
[36] Walker J A 1998 Estimating velocities and accelerations of animal locomotion: a simulation experiment comparing numerical differentiation algorithms *J. Exp. Biol.* **201** 981–95
[37] Ern P, Risso F, Fabre D and Magnaudet J 2012 Wake-induced oscillatory paths of bodies freely rising or falling in fluids *Annu. Rev. Fluid Mech.* **44** 97–121
[38] Heisinger L, Newton P and Kanso E 2014 Coins falling in water *J. Fluid Mech.* **742** 243–53
[39] Vincent L, Scott Shambaugh W and Kanso E 2016 Holes stabilize freely falling coins *J. Fluid Mech.* **801** 250–9
[40] Stafford B J, Thorington R W Jr and Kawamichi T 2002 Gliding behavior of Japanese giant flying squirrels (*Petaurista leucogenys*) *J. Mammal.* **83** 553–62
[41] O'Dor R, Stewart J, Gilly W, Payne J, Borges T C and Thys T 2013 Squid rocket science: how squid launch into air *Deep-Sea Res* II **95** 113–8
[42] Socha J J and LaBarbera M 2005 Effects of size and behavior on aerial performance of two species of flying snakes (*Chrysopelea*) *J. Exp. Biol.* **208** 1835–47
[43] Chatterjee S and Jack Templin R 2007 Biplane wing planform and flight performance of the feathered dinosaur *Microraptor gui Proc. Natl Acad. Sci. USA* **104** 1576–80
[44] Evangelista D, Cardona G, Guenther-Gleason E, Huynh T, Kwong A, Marks D, Ray N, Tisbe A, Tse K and Koehl M 2014 Aerodynamic characteristics of a feathered dinosaur measured using physical models. Effects of form on static stability and control effectiveness *PLoS One* **9** e85203

Supplemental Information

Global dynamics of non-equilibrium gliding in animals

Isaac J. Yeaton[1,*], John J. Socha[2] and Shane D. Ross[2]

[1]Department of Mechanical Engineering
[2]Department of Biomedical Engineering and Mechanics
Virginia Tech
[*]Corresponding author: iyeaton@vt.edu

March 1, 2017

Code repository

Python code to reproduce figures in the manuscript, including velocity polar diagrams and pitch bifurcation diagrams, can be found at
`https://github.com/TheSochaLab/Global-dynamics-of-non-equilibrium-gliding-in-animals`.

1 Linear stability analysis

The Jacobian of the polar coordinate equations (2.7) and (2.8) in the main text, evaluated at equilibrium is

$$A_{(\gamma^*,\hat{v}^*)} = \begin{bmatrix} \dfrac{\partial \gamma'}{\partial \gamma} & \dfrac{\partial \gamma'}{\partial \hat{v}} \\ \dfrac{\partial \hat{v}'}{\partial \gamma} & \dfrac{\partial \hat{v}'}{\partial \hat{v}} \end{bmatrix}_{(\gamma^*,\hat{v}^*)} \tag{1.1}$$

After simplification, the partial derivatives are

$$\frac{\partial \gamma'}{\partial \gamma} = -\frac{(C_L' + C_D)}{(C_L^2 + C_D^2)^{1/4}} \qquad \frac{\partial \gamma'}{\partial \hat{v}} = -2C_L$$
$$\frac{\partial \hat{v}'}{\partial \gamma} = \frac{C_L - C_D'}{(C_L^2 + C_D^2)^{1/2}} \qquad \frac{\partial \hat{v}'}{\partial \hat{v}} = \frac{-2C_D}{(C_L^2 + C_D^2)^{1/4}}$$

where the lift and drag coefficient values, as well as their slopes C_L' and C_D', are evaluated at the equilibrium angle of attack in radians.

Common types of equilibrium points can be calculated analytically. Saddle point equilibria occur when

$$(C_L/C_D)' < -\left[1 + (C_L/C_D)^2\right]$$

and stable equilibria occur when

$$C_L' > -3C_D.$$

Lastly, the equilibrium glide velocities at any equilibrium are

$$\hat{v}^* = (C_L^2 + C_D^2)^{-1/4} \qquad \hat{v}_x^* = \hat{v}^* \cos\gamma^* \qquad \hat{v}_z^* = -\hat{v}^* \sin\gamma^*. \tag{1.2}$$

2 Conversion between dimensional, non-dimensional, and rescaled quantities

Below we list the conversion from dimensional quantities, non-dimensional quantities (with the overbar), and rescaled quantities (with an overhat).

$$t = \sqrt{\frac{c}{g\epsilon}}\hat{t} \qquad x = \frac{c}{\epsilon}\hat{x} \qquad v = \sqrt{\frac{cg}{\epsilon}}\hat{v} \qquad a = g\hat{a} \tag{2.1}$$

$$t = \sqrt{\frac{c}{g}}\bar{t} \qquad x = c\bar{x} \qquad v = \sqrt{cg}\bar{v} \qquad a = g\bar{a} \tag{2.2}$$

$$\bar{t} = \frac{\hat{t}}{\sqrt{\epsilon}} \qquad \bar{x} = \frac{\hat{x}}{\epsilon} \qquad \bar{v} = \frac{\hat{v}}{\sqrt{\epsilon}} \qquad \bar{a} = \hat{a} \tag{2.3}$$

The universal glide scaling parameter,

$$\epsilon = \frac{\rho c}{2}\frac{S}{m} = \frac{\rho g}{2}\frac{c}{W_S} \tag{2.4}$$

when substituted back into the rescaled terms, results in the wing loading expression in the main text (equation 4.1):

$$t = \sqrt{\frac{2W_S}{\rho g^2}}\hat{t} \qquad x = \frac{2W_S}{\rho g}\hat{x} \qquad v = \sqrt{\frac{2W_S}{\rho}}\hat{v} \qquad a = g\hat{a} \tag{2.5}$$

The time, length, and velocity, and acceleration scales are thus

$$T = \sqrt{\frac{2W_S}{\rho g^2}} \qquad L = \frac{2W_S}{\rho g} \qquad \frac{L}{T} = \sqrt{\frac{2W_S}{\rho}} \qquad \frac{L}{T^2} = g \tag{2.6}$$

3 Velocity polar diagram when C_L and C_D are constant

When the lift and drag coefficients are constants, only stable equilibria are possible. Additionally, they are of spiral type when the lift-to-drag ratio is less that 0.354. Below is a velocity polar diagram constructed using lift and drag coefficients values report in Socha *et. al* (2010), table 1, for one configuration used in their simulations. We use 'Case 6: Average' with $C_L = .54$, $C_D = .29$, and $C_L/C_D = 1.88$. They also proposed a definition of equilibrium based on when the glide angle reaches 5% of its asymptotic value; this range is also indicated on the velocity polar diagram.

As is clear, there is strong spiraling behavior around a stable focus equilibrium point. As indicated in figure 3 in the main text, this equilibrium point is far from the boundary between a node and a focus. Additionally, the velocity polar diagram indicates that all initial conditions will lead to a stable glide and that the low acceleration magnitude region is confined around the equilibrium point.

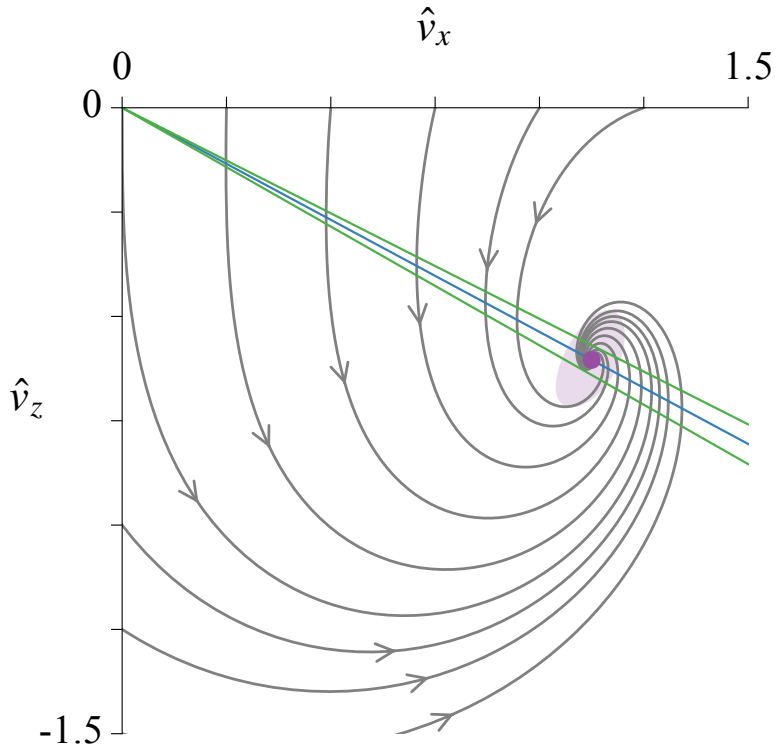

Figure 1: Velocity polar diagram for constant lift and drag coefficients. The equilibrium condition proposed by Socha *et. al* (2010).

4 Kinematic lift and drag coefficient curves

Here we derive the lift and drag force from the horizontal and vertical forces. The lift and drag force are then used to calculate the lift and drag coefficients. We beginning with the horizontal and vertical forces:

$$F_x = ma_x = F_L \sin\gamma - F_D \cos\gamma$$
$$F_z = ma_z = F_L \cos\gamma + F_D \sin\gamma - mg$$

To calculate the lift force, we multiply the x-equation by $\sin\gamma$ and the z-equation by $\cos\gamma$ and sum. This gives

$$\begin{aligned} F_x \sin\gamma + F_z \cos\gamma =& F_L(\sin^2\gamma + \cos^2\gamma) + \\ & F_D(\cos\gamma \sin\gamma - \cos\gamma \sin\gamma) - mg\cos\gamma, \end{aligned}$$

which simplifies to

$$F_L = F_x \sin\gamma + F_z \cos\gamma + mg\cos\gamma.$$

To obtain the drag force, we multiply the x-equation by $-\cos\gamma$ and the z-equation by $\sin\gamma$ and sum. This gives

$$\begin{aligned} -F_x \cos\gamma + F_z \sin\gamma =& F_L(\cos\gamma \sin\gamma - \cos\gamma \sin\gamma) + \\ & F_D(\sin^2\gamma + \cos^2\gamma)) - mg\sin\gamma, \end{aligned}$$

which simplifies to,

$$F_D = -F_x \cos\gamma + F_z \sin\gamma + mg\sin\gamma.$$

The lift and drag coefficients become

$$C_L(\gamma + \theta_b) = \frac{ma_x \sin\gamma + ma_z \cos\gamma + mg\cos\gamma}{\frac{1}{2}\rho v^2 S}$$
$$C_D(\gamma + \theta_b) = \frac{-ma_x \cos\gamma + ma_z \sin\gamma + mg\sin\gamma}{\frac{1}{2}\rho v^2 S}$$

The lift and drag coefficients have been written with explicit dependence on both glide angle and body pitch angle θ_b. The glide angle is calculated at each measurement location as $\gamma = -\tan^{-1} v_z/v_x$, but the body pitch angle is not accessible from the kinematics data and must be estimated throughout the entire glide. The body pitch angle was specified to be 0° such that the animal is horizontal to the ground. Short glides presented in [1] of *Glaucomys volans* showed a pitch angle tending towards 0°.

Individual squirrel glide trials presented in the data supplement of [2] were reanalyzed for this study. The data set consists of 59 glides of wild northern flying squirrel (*Glaucomys sabrinus*). A

majority of trials, 23 of 59, landed on a tree 18 m from the launch site. We analyze these glides because they were analyzed in detail by in ref. [2] and because longer glides give more opportunity to reach equilibrium. Individual squirrels were not marked, so analyses were performed using an average size squirrel based on previous studies. Therefore, we are calculating 'equivalent' lift and drag curves.

Of the 18 m glides, we further restrict the data set to 14 trajectories based on the start and end positions. We require the initial recorded position to be within 3.8 m horizontally and 2 m vertically from the jump point. We also require the trajectories to end with a horizontal distance between 16 m to 18.5 m. These values were selected to ensure the longest possible glides and to capture as much of the transient portion as possible. Note that most of the ballistic phase of the trajectory was not recorded in the original data set.

Velocities and accelerations are calculated using a moving window procedure similar to [2]. Velocities are calculated by iterating through the individual position components and fitting a linear polynomial to the window. The derivative of the window polynomial is evaluated at the current time to calculate velocity. Acceleration was calculated in a similar way, using the velocity time series as input. A half-window is used at the start and end of each time series. The half-window grows until it reaches the set window size. The variable window size increased derivative scatter if a higher-order polynomial was used. This was especially noticeable at the end of the trajectory where reported digitzation errors are largest. For all trials, a total window of 81 points, or 0.64 sec, was used. This window uses 40 points before and after the current time step. A large interrogation window was used to obtain the bulk glide performance and smooth out small corrections to the trajectory [2]. Lift and drag coefficient curves were calculated as described above, as was the lift-to-drag ratio. There was significant scatter in the lift and drag curves at small glide angles and therefore angles of attack. This occurred late in the glide, where digitization error was highest. We therefore restricted these curves to start at 10°, and performed glide angle binning from 10° to 44° in 2° increments. Next, a third-order spline was fit to the individual lift and drag coefficient curves. The scatter and binning is shown in figure 2.

Mean kinematic lift-to-drag ratio curves were calculated by aggregating all glide trials for a particular species. Because glide angle varied continuously during glides, points within a defined glide angle range were averaged. A Taylor moment expansion was used to find the mean and variance of the lift-to-drag-ratio [3, 4]. Naively taking the ratio of lift coefficient to drag coefficient will result in a biased ratio. We use a Taylor series expansion to find the mean and variance of the lift-to-drag ratio in each glide angle bin using

$$
\begin{aligned}
E\left[\frac{C_L(\alpha_b)}{C_D(\alpha_b)}\right] &\approx E\left[\frac{C_L(\alpha_b)}{C_D(\alpha_b)}\right] - \frac{\mathrm{cov}[C_L(\alpha_b), C_D(\alpha_b)]}{E[C_D(\alpha_b)]^2} + \frac{E[C_L(\alpha_b)]}{E[C_D(\alpha_b)]^3}\mathrm{var}[C_D(\alpha_b)] \\
\mathrm{var}\left[\frac{C_L(\alpha_b)}{C_D(\alpha_b)}\right] &\approx \frac{\mathrm{var}[C_L(\alpha_b)]}{E[C_D(\alpha_b)]^2} - \frac{2E[C_L(\alpha_b)]}{E[C_D(\alpha_b)]^3}\mathrm{cov}[C_L(\alpha_b), C_D(\alpha_b)] \\
&\quad + \frac{E[C_L(\alpha_b)]^2}{E[C_D(\alpha_b)]^4}\mathrm{var}[C_D(\alpha_b)]
\end{aligned}
$$

where $\alpha_b = \gamma + \theta_b$ and $\text{cov}[C_L(\alpha_b), C_D(\alpha_b)]$ is the covariance.

Although the kinematic method of determining aerodynamic coefficients is not ideal, it does provide a measure of the coefficient curves of gliders in their natural setting. Similar techniques have been used for small fixed-wing gliders [5, 6] where multiple markers were placed on the glider, position data differentiated, and aerodynamic parameter calculated. However, this is an idealization of the experimental data available here, including the mass distribution of animal gliders, unsteady fluid mechanics, varying wing size and shape, and time-varying mass distribution.

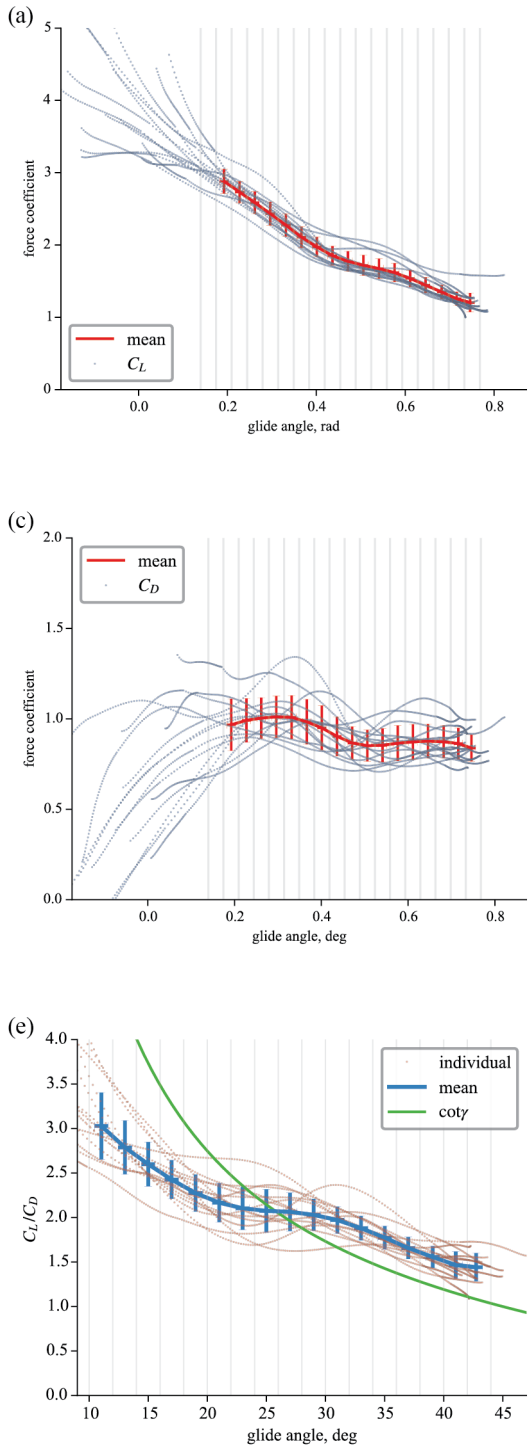

Figure 2: Mean kinematics-based lift, drag, and lift-to-drag ratio coefficient curves.

5 Numerical implementation of Velocity Polar Diagrams

Velocity polar diagrams are constructed by integrating the Cartesian equations of motion for initial conditions $(\hat{v}_{0,x}, \hat{v}_{0,z})$ along the perimeter of the velocity space. This technique requires 1) spline fits of the lift and drag coefficients, 2) the measured angle of attack range, and 3) the specified pitch angle of the glider. The horizontal and vertical velocity initial conditions are specified such that $\alpha_{\min} < \gamma_0 - \theta < \alpha_{\max}$, where $\gamma_0 = -\tan^{-1} \hat{v}_{0,z}/\hat{v}_{0,x}$. This results in the wedge shape of some velocity polar diagrams. Trajectories are found by integrating the equations forward in time using a variable time step fifth-order accurate Dormand-Prince ODE solver until one of the following conditions is met: the angle of attack exceeded the experimentally recorded range; the solver integrates for a total non-dimensional time of 30; or the velocity trajectory leaves the bounding box $\hat{v}_x \in [0, 1.25]$, $\hat{v}_z \in [0, -1.25]$. Each trajectory is then plotted to show the phase space flow.

Equilibrium points are found as described in the main text and plotted on the velocity polar diagram. The stable and unstable branches (separatrices) of saddle point equilibria are found by integrating trajectories forward and backwards in time for four initial conditions surrounding the saddle, offset by ± 0.0001. The backwards integration identifies the unstable branches and the forward integration specifies the stable branches. Finally, low acceleration regions and nullclines are found by evaluating the Cartesian equations of motion on a fine grid and then plotting contour plots for the following conditions: $|a| < 0.1$ and $\hat{v}_z' = 0$.

6 Stability Analysis and Terminal Velocity Manifold Computation

Below we list the analytical calculation of the terminal velocity manifold and details about the Hopf bifurcation.

The equilibrium condition implies

$$\begin{aligned}
\bar{v}^* &= \frac{1}{\left(C_L(\alpha^*)^2 + C_D(\alpha^*)^2\right)^{1/4}} \\
\gamma^* &= \cot^{-1}\left(\frac{C_L(\alpha^*)}{C_D(\alpha^*)}\right) \\
\bar{v}_x^* &= \quad \bar{v}^* \cos\gamma^* \\
\bar{v}_z^* &= -\bar{v}^* \sin\gamma^* \\
\alpha^* &= \theta + \gamma^*
\end{aligned}$$

6.1 Expansion about the equilibrium

In order to obtain an analytical approximation of the eigenvalues and eigenvectors, and to put the system in a form where we can analytically obtain the glide manifold in the snake phase space, we first do a change of coordinates centered on an equilibrium point. We will work in polar coordinates,

since the equations of motion look simpler,

$$\psi = \gamma - \gamma^*, \qquad r = \bar{v} - \bar{v}^* \tag{6.1}$$

where we are working in non-dimensional and rescaled variables. At equilibrium we know

$$\begin{aligned} \hat{v}' = 0 &\Rightarrow \bar{v}^{*2} C_D(\alpha) = \sin\gamma^* \\ \gamma' = 0 &\Rightarrow \bar{v}^{*2} C_L(\alpha) = \cos\gamma^*. \end{aligned} \tag{6.2}$$

In the shifted coordinates, the equilibrium is the origin and the equations of motion are

$$\begin{aligned} \psi' &= -(\bar{v}^* + r) C_L(\gamma^* + \theta^* + \varphi + \psi) + \frac{1}{(\bar{v}^* + r)} \cos(\gamma^* + \psi), \\ r' &= -(\bar{v}^* + r)^2 C_D(\gamma^* + \theta^* + \varphi + \psi) + \sin(\gamma^* + \psi), \end{aligned} \tag{6.3}$$

We want to write the right-hand-side of the equations of motion as a power series expansion in ψ and r. To start out, we will get this expansion to second-order.

Let's first look at the ψ' expression. Note that, via Taylor expansion,

$$\frac{1}{(\bar{v}^* + r)} = \frac{1}{\bar{v}^* \left(1 + \frac{r}{\bar{v}^*}\right)} = \frac{1}{\bar{v}^*} \left(1 - \frac{r}{\bar{v}^*} + \left(\frac{r}{\bar{v}^*}\right)^2 - \left(\frac{r}{\bar{v}^*}\right)^3 + \mathcal{O}\left(\frac{r}{\bar{v}^*}\right)^4\right) \tag{6.4}$$

Using the cos addition formula,

$$\cos(\gamma^* + \psi) = \cos\psi \cos\gamma^* - \sin\psi \sin\gamma^* \tag{6.5}$$

along with (6.2), we get

$$\begin{aligned} \frac{1}{\bar{v}^*} \cos(\gamma^* + \psi) &= \frac{1}{\bar{v}^*} \left[\bar{v}^{*2} C_L(\alpha^*) \cos\psi - \bar{v}^{*2} C_D(\alpha^*) \sin\psi\right] \\ &= \bar{v}^* \left[C_L(\alpha^*) \cos\psi - C_D(\alpha^*) \sin\psi\right] \end{aligned} \tag{6.6}$$

so,

$$\begin{aligned} \frac{1}{(\bar{v}^* + r)} \cos(\gamma^* + \psi) &= \bar{v}^* \left[C_L(\alpha^*) \cos\psi - C_D(\alpha^*) \sin\psi\right] \left(1 - \frac{r}{\bar{v}^*} + \left(\frac{r}{\bar{v}^*}\right)^2 - \left(\frac{r}{\bar{v}^*}\right)^3 + \mathcal{O}\left(\frac{r}{\bar{v}^*}\right)^4\right) \\ &= \bar{v}^* \left[C_L(\alpha^*) \cos\psi - C_D(\alpha^*) \sin\psi\right] - r \left[C_L(\alpha^*) \cos\psi - C_D(\alpha^*) \sin\psi\right] \\ &+ \left(\frac{r^2}{\bar{v}^*} - \frac{r^3}{\bar{v}^{*2}}\right) \left[C_L(\alpha^*) \cos\psi - C_D(\alpha^*) \sin\psi\right] + \mathcal{O}\left(r^4\right) \end{aligned} \tag{6.7}$$

Also note that $C_L(\gamma^* + \theta^* + \varphi + \psi) = C_L(\alpha^* + \psi)$, and by Taylor series expansion we have

$$C_L(\alpha^* + \psi) = C_L(\alpha^*) + \psi C_L'(\alpha^*) + \tfrac{1}{2}\psi^2 C_L''(\alpha^*) + \mathcal{O}(\psi^3) \tag{6.8}$$

and similarly for the drag term,

$$C_D(\alpha^* + \psi) = C_D(\alpha^*) + \psi C_D'(\alpha^*) + \tfrac{1}{2}\psi^2 C_D''(\alpha^*) + \tfrac{1}{6}\psi^3 C_D'''(\alpha^*) + \mathcal{O}(\psi^4) \tag{6.9}$$

so,

$$\begin{aligned} -(\bar{v}^* + r)C_L(\gamma^* + \theta^* + \varphi + \psi) = &-\bar{v}^* \left[C_L(\alpha^*) + \psi C_L'(\alpha^*) + \tfrac{1}{2}\psi^2 C_L''(\alpha^*) + \tfrac{1}{6}\psi^3 C_D'''(\alpha^*) + \mathcal{O}(\psi^4)\right] \\ &- r\left[C_L(\alpha^*) + \psi C_L'(\alpha^*) + \tfrac{1}{2}\psi^2 C_L''(\alpha^*) + \mathcal{O}(\psi^3)\right] \end{aligned} \tag{6.10}$$

So the ψ' expression becomes

$$\begin{aligned} \psi' = &\bar{v}^* \left(-C_L(\alpha^* + \psi) + C_L(\alpha^*)\cos\psi - C_D(\alpha^*)\sin\psi\right) \\ &+ r\left(-C_L(\alpha^* + \psi) - C_L(\alpha^*)\cos\psi + C_D(\alpha^*)\sin\psi\right) \\ &+ \left(\frac{r^2}{\bar{v}^*} - \frac{r^3}{\bar{v}^{*2}}\right)\left[C_L(\alpha^*)\cos\psi - C_D(\alpha^*)\sin\psi\right] + \mathcal{O}\left(r^4\right) \end{aligned} \tag{6.11}$$

Note the Taylor series up to 3rd order in ψ for cos and sin is,

$$\cos\psi = 1 - \tfrac{1}{2}\psi^2 + \mathcal{O}(\psi^4), \qquad \sin\psi = \psi - \tfrac{1}{6}\psi^3 + \mathcal{O}(\psi^5)$$

Plugging in all the Taylor series expansions, we get, up through 3rd order in ψ and r,

$$\begin{aligned} \psi' = &\bar{v}^* \left(-C_L - \psi C_L' - \tfrac{1}{2}\psi^2 C_L'' - \tfrac{1}{6}\psi^3 C_D''' + C_L - \tfrac{1}{2}\psi^2 C_L - \psi C_D + \tfrac{1}{6}\psi^3 C_D\right) \\ &+ r\left(-C_L - \psi C_L' - \tfrac{1}{2}\psi^2 C_L'' - C_L + \tfrac{1}{2}\psi^2 C_L + C_D\psi\right) \\ &+ \left(\frac{r^2}{\bar{v}^*} - \frac{r^3}{\bar{v}^{*2}}\right)\left[C_L - C_D\psi\right] + \mathcal{O}\left(4\right) \end{aligned} \tag{6.12}$$

where it should be understood that the lift and drag coefficients and all their derivatives (w.r.t. angle of attack) are evaluated at the critical point α^*, and where $\mathcal{O}(4)$ stands for terms which are fourth order or higher in the variables ψ and r.

Grouping terms by powers in ψ and r, we get

$$\begin{aligned} \psi' = &\bar{v}^* \left[-C_L' - C_D\right]\psi + 2\left[-C_L\right] r \\ &+ \tfrac{\bar{v}^*}{2}\left[-C_L'' - C_L\right]\psi^2 + \left[-C_L' + C_D\right]\psi r + \tfrac{1}{\bar{v}^*}[C_L]r^2 \\ &+ \tfrac{\bar{v}^*}{6}[C_D - C_L''']\psi^3 + \tfrac{1}{2}[C_L - C_L'']\psi^2 r + \tfrac{1}{\bar{v}^*}[-C_D]\psi r^2 + \tfrac{1}{\bar{v}^{*2}}[-C_L]r^3 + \mathcal{O}(4) \end{aligned} \tag{6.13}$$

There are terms linear in ψ and r, terms second-order in ψ and r, and terms third-order in ψ and r.

We can follow a similar procedure for the r' expression. Using the sin addition formula,

$$\sin(\gamma^* + \psi) = \sin\psi\cos\gamma^* + \cos\psi\sin\gamma^* \tag{6.14}$$

along with (6.2), we get

$$\begin{aligned}\sin(\gamma^* + \psi) &= \left[\bar{v}^{*2} C_L \sin\psi + \bar{v}^{*2} C_D \cos\psi\right] \\ &= \bar{v}^{*2}\left[C_L \sin\psi + C_D \cos\psi\right] \\ &= \bar{v}^{*2}\left[C_L\psi - \tfrac{1}{6}C_L\psi^3 + C_D - \tfrac{1}{2}\psi^2 C_D + \mathcal{O}(4)\right]\end{aligned} \tag{6.15}$$

Also,

$$\begin{aligned}-(\bar{v}^* + r)^2 C_D(\alpha^* + \psi) = &-\bar{v}^{*2}\left[C_D + \psi C_D' + \tfrac{1}{2}\psi^2 C_D'' + \tfrac{1}{6}\psi^3 C_D''' + \mathcal{O}(4)\right] \\ &- 2\bar{v}^* r\left[C_D + \psi C_D' + \tfrac{1}{2}\psi^2 C_D'' + \mathcal{O}(3)\right] \\ &- r^2\left[C_D + \psi C_D' + \mathcal{O}(2)\right]\end{aligned} \tag{6.16}$$

so we get

$$\begin{aligned}r' = &\bar{v}^{*2}\left[-C_D' + C_L\right]\psi + 2\left[-\bar{v}^* C_D\right] r \\ &+ \tfrac{\bar{v}^{*2}}{2}\left[-C_D - C_D''\right]\psi^2 + 2\bar{v}^*[-C_D']\psi r + [-C_D] r^2 \\ &+ \tfrac{\bar{v}^{*2}}{6}[-C_L - C_D''']\psi^3 + \bar{v}^*[-C_D'']\psi^2 r + \tfrac{1}{2}[-C_D']\psi r^2 + [0] r^3 + \mathcal{O}(4)\end{aligned} \tag{6.17}$$

Putting the (ψ, r) system into matrix form, we have

$$\begin{bmatrix}\psi' \\ r'\end{bmatrix} = \underbrace{\begin{bmatrix}\bar{v}^*\left[-C_L' - C_D\right] & [-2C_L] \\ \bar{v}^{*2}\left[-C_D' + C_L\right] & [-2\bar{v}^* C_D]\end{bmatrix}}_{\mathbf{A}} \begin{bmatrix}\psi \\ r\end{bmatrix} + \mathbf{F}(\psi, r) + \mathcal{O}(4) \tag{6.18}$$

where $\mathbf{F}(\psi, r)$ stands for second and third-order terms, and is given by

$$\mathbf{F}(\psi, r) = \begin{bmatrix}F^1(\psi, r) \\ F^2(\psi, r)\end{bmatrix} \tag{6.19}$$

where

$$\begin{aligned}F^1(\psi, r) = &\tfrac{\bar{v}^*}{2}\left[-C_L - C_L''\right]\psi^2 + \left[C_D - C_L'\right]\psi r + \tfrac{1}{\bar{v}^*}[C_L] r^2 \\ &+ \tfrac{\bar{v}^*}{6}[C_D - C_L''']\psi^3 + \tfrac{1}{2}[C_L - C_L'']\psi^2 r + \tfrac{1}{\bar{v}^*}[-C_D]\psi r^2 + \tfrac{1}{\bar{v}^{*2}}[-C_L] r^3\end{aligned} \tag{6.20}$$

and

$$\begin{aligned}F^2(\psi, r) = &\tfrac{\bar{v}^{*2}}{2}\left[-C_D - C_D''\right]\psi^2 + 2\bar{v}^*[-C_D']\psi r + [-C_D] r^2 \\ &+ \tfrac{\bar{v}^{*2}}{6}[-C_L - C_D''']\psi^3 + \bar{v}^*[-C_D'']\psi^2 r + \tfrac{1}{2}[-C_D']\psi r^2 + [0] r^3\end{aligned} \tag{6.21}$$

From the 2×2 linearization matrix $\mathbf{A}$ in (6.18),

$$\mathbf{A} = \begin{bmatrix}\bar{v}^*\left[-C_L' - C_D\right] & [-2C_L] \\ \bar{v}^{*2}\left[-C_D' + C_L\right] & [-2\bar{v}^* C_D]\end{bmatrix} \tag{6.22}$$

(also given in appendix A), we can analytically determine the eigenvalues and eigenvectors in terms of the equilibrium point and characteristics of the lift and drag curves at that point.

For this simple system, we can write the eigenvalue equation in the standard form as [7, p. 130]

$$\lambda^2 - \bar{\tau}\lambda + \bar{\Delta} = 0,$$

where $\bar{\tau} = \text{trace}(\mathbf{A})$ and $\bar{\Delta} = \det(\mathbf{A})$. The eigenvalues are

$$\lambda_1 = \frac{\bar{\tau} + \sqrt{\bar{\tau}^2 - 4\bar{\Delta}}}{2}, \qquad \lambda_2 = \frac{\bar{\tau} - \sqrt{\bar{\tau}^2 - 4\bar{\Delta}}}{2}$$

The trace of $\mathbf{A}$ is

$$\bar{\tau} = \bar{v}^* \left[-C_L' - 3C_D\right]$$

and the determinant of $\mathbf{A}$ is

$$\bar{\Delta} = 2\bar{v}^{*2} \left[C_L^2 + C_D^2 + C_L' C_D - C_D' C_L\right]$$

So,

$$\begin{aligned} \bar{\tau}^2 - 4\bar{\Delta} &= \bar{v}^{*2} \left[(C_L' + 3C_D)^2 - 8(C_L^2 + C_D^2 + C_L' C_D - C_D' C_L)\right] \\ &= \bar{v}^{*2} \left[C_L'^2 + C_D^2 - 2C_L' C_D - 8C_L^2 + 8C_D' C_L\right] \\ &= \bar{v}^{*2} \left[(C_D - C_L')^2 - 8C_L(C_L - C_D')\right] \end{aligned} \tag{6.23}$$

and the eigenvalues are

$$\lambda_{1,2} = \frac{\bar{\tau} \pm \sqrt{\bar{\tau}^2 - 4\bar{\Delta}}}{2}$$

We can write the eigenvalues more compactly by introducing τ and Δ,

$$\begin{aligned} \tau &= (C_L'/C_D) + 3 \\ \Delta &= (C_L/C_D)' + (C_L/C_D)^2 + 1 \end{aligned} \tag{6.24}$$

such that

$$\begin{aligned} \bar{\tau} &= -\frac{C_D}{(C_L^2 + C_D^2)^{1/4}}\tau \\ \bar{\Delta} &= 2\frac{C_D^2}{(C_L^2 + C_D^2)^{1/2}}\Delta \end{aligned} \tag{6.25}$$

in which case,

$$\lambda_{1,2} = \frac{C_D}{2(C_L^2 + C_D^2)^{1/4}} \left(-\tau \pm \sqrt{\tau^2 - 8\Delta}\right) \tag{6.26}$$

and since the prefactor

$$\frac{C_D}{2(C_L^2 + C_D^2)^{1/4}} \tag{6.27}$$

is always a positive scalar, the location of the eigenvalues on the complex plane is given solely by τ and Δ.

6.2 Hopf bifurcation case

We often view the pitch variable θ as a bifurcation parameter. A Hopf bifurcation occurs when $\bar{\tau} = 0$ and $\bar{\Delta} > 0$, so the eigenvalues are purely imaginary,

$$\lambda_{\pm} = \pm i\omega$$

where $\omega = \sqrt{\bar{\Delta}} > 0$. Suppose this occurs along the branch of equilibria at a particular value of θ which we'll call $\bar{\theta}$. By the assumption of $\bar{\tau} = 0$, we conclude that

$$C_L' = -3C_D \tag{6.28}$$

and from $\bar{\Delta} > 0$, we conclude that

$$C_L > \tfrac{1}{2}\left(C_D' + \sqrt{C_D'^2 + 8C_D^2}\right) \quad \text{or} \quad \mathrm{C_L} < \tfrac{1}{2}\left(\mathrm{C_D'} - \sqrt{\mathrm{C_D'^2 + 8C_D^2}}\right) \tag{6.29}$$

Notice that the sign of

$$d = \frac{d}{d\theta}\left(\mathrm{Re}(\lambda(\theta))\right)\Big|_{\theta=\bar{\theta}} = \tfrac{1}{2}\bar{\tau}' = \tfrac{1}{2}\bar{v}^*(-C_L'' - 3C_D') \tag{6.30}$$

is an indication of the type of bifurcation. If, as θ increases, the equilibrium point is going from a stable to unstable focus, then $\bar{\tau}' > 0$. Otherwise, $\bar{\tau}' < 0$. Note that

$$\begin{aligned} C_L'' &< -3C_D' \quad \text{going from stable to unstable}, \bar{\tau}' > 0 \\ C_L'' &> -3C_D' \quad \text{going from unstable to stable}, \bar{\tau}' < 0 \end{aligned} \tag{6.31}$$

For the case of purely imaginary eigenvalues, we have

$$\mathbf{A} = \begin{bmatrix} \bar{v}^* 2C_D & -2C_L \\ \bar{v}^{*2}\left(-C_D' + C_L\right) & -\bar{v}^* 2C_D \end{bmatrix} \tag{6.32}$$

where the eigenvalues are $\pm i\omega$, where

$$\omega = \bar{v}^*\sqrt{2}\sqrt{C_L^2 - C_L C_D' - 2C_D^2} \tag{6.33}$$

is positive. We solve for the generalized eigenvectors $\mathbf{u}$ and $\mathbf{v}$,

$$\mathbf{u} = \begin{bmatrix} 2C_L \\ \bar{v}^* 2C_D \end{bmatrix} \quad \mathbf{v} = \begin{bmatrix} 0 \\ \omega \end{bmatrix} \tag{6.34}$$

Define the matrix $\mathbf{P}$ as

$$\mathbf{P} = [\mathbf{u} \;\; \mathbf{v}]$$

so $\mathbf{u}$ is the first column of $\mathbf{P}$ and $\mathbf{v}$ is the second column of $\mathbf{P}$. This matrix defines a linear transformation to the eigenbasis (x, y) via

$$\begin{bmatrix} \psi \\ r \end{bmatrix} = \mathbf{P} \begin{bmatrix} x \\ y \end{bmatrix}$$

so the x coordinate is along the $\mathbf{u}$ direction and the y coordinate is along the $\mathbf{v}$ direction. Note that

$$\begin{aligned} \psi &= 2C_L x \\ r &= \bar{v}^* 2C_D x + \omega y \end{aligned} \tag{6.35}$$

The dynamics in the eigenbasis are

$$\begin{bmatrix} x' \\ y' \end{bmatrix} = \begin{bmatrix} 0 & -\omega \\ \omega & 0 \end{bmatrix} \begin{bmatrix} x \\ y \end{bmatrix} + \mathbf{P}^{-1}\mathbf{F}(2C_L x, \bar{v}^* 2C_D x + \omega y) + \mathcal{O}(4) \tag{6.36}$$

where $\mathbf{F}$, from (6.19), includes the 2nd and 3rd order terms and where

$$\mathbf{P}^{-1} = \begin{bmatrix} \frac{1}{2C_L} & 0 \\ -\frac{\bar{v}^* C_D}{\omega C_L} & \frac{1}{\omega} \end{bmatrix} \tag{6.37}$$

We will re-write the nonlinear terms, defining $\mathbf{f}(x, y) = \mathbf{P}^{-1}\mathbf{F}(2C_L x, \bar{v}^* 2C_D x + \omega y)$, so the resulting equation now has the form,

$$\begin{bmatrix} x' \\ y' \end{bmatrix} = \begin{bmatrix} 0 & -\omega \\ \omega & 0 \end{bmatrix} \begin{bmatrix} x \\ y \end{bmatrix} + \begin{bmatrix} f^1(x, y) \\ f^2(x, y) \end{bmatrix} \tag{6.38}$$

The coefficient a, from [8] and [9], which determines what kind of Hopf bifurcation will occur, can be calculated as

$$\begin{aligned} a = &\tfrac{1}{16}\left[f^1_{xxx} + f^1_{xyy} + f^2_{xxy} + f^2_{yyy}\right] \\ &+ \tfrac{1}{16\omega}\left[f^1_{xy}(f^1_{xx} + f^1_{yy}) - f^2_{xy}(f^2_{xx} + f^2_{yy}) - f^1_{xx}f^2_{xx} + f^1_{yy}f^2_{yy}\right] \end{aligned} \tag{6.39}$$

where all partial derivatives are evaluated at the bifurcation point, $\theta = \bar{\theta}$, $x = 0$, $y = 0$,

$$\begin{aligned}
F^1_{xx} &= \bar{v}^*(4{C_L}^3 - 4{C_L}^3 C''_L + 36 C_L {C_D}^2) \\
F^1_{xy} &= \omega 12 C_L C_D \\
F^1_{yy} &= \bar{v}^* 4 C_L({C_L}^2 - C_L C'_D - 2{C_D}^2) \\
F^2_{xx} &= -\bar{v}^{*2}(4{C_L}^2 C_D + 8{C_D}^3 + 4{C_L}^2 C''_D + 16 C_L C_D C'_D) \\
F^2_{xy} &= -\bar{v}^* \omega(C_L C'_L + {C_D}^2) \\
F^2_{yy} &= -\bar{v}^{*2} 4 C_D({C_L}^2 - C_L C'_D - 2{C_D}^2) \\
F^1_{xxx} &= -\bar{v}^*(8{C_L}^3 C'''_L + 24{C_L}^2 C_D C''_L + 96 C_L {C_D}^3 - 32{C_L}^3 C_D) \\
F^1_{xyy} &= -\bar{v}^* 32 C_D C_L({C_L}^2 - C_L C'_D - 2{C_D}^2) \\
F^1_{xxy} &= \bar{v}^*(4[C_L - C''_L]{C_L}^2(\tfrac{\omega}{\bar{v}^*}) - 40 C_L {C_D}^2(\tfrac{\omega}{\bar{v}^*})) \\
F^1_{yyy} &= -\bar{v}^* 12 C_L({C_L}^2 - C_L C'_D - 2{C_D}^2)(\tfrac{\omega}{\bar{v}^*}) \\
F^2_{xxy} &= -\bar{v}^* \omega(8{C_L}^2 C''_D + 8 C_L C_D C'_D) \\
F^2_{yyy} &= 0
\end{aligned} \tag{6.40}$$

and we get the partial derivatives of $\mathbf{f}(x, y)$ from the relationship

$$\mathbf{f}(x, y) = \mathbf{P}^{-1}\mathbf{F}(x, y)$$

which give us

$$\begin{aligned}
f^1(x, y) &= \tfrac{1}{2C_L} F_1(x, y) \\
f^2(x, y) &= -\tfrac{\bar{v}^* C_D}{\omega C_L} F_1(x, y) + \tfrac{1}{\omega} F_2(x, y)
\end{aligned} \tag{6.41}$$

Knowing the sign of a along with the sign of τ' will determine which of the four cases of Hopf bifurcation is present, via the Poincaré-Andronov-Hopf Bifurcation Theorem ([8]).

For example, for the pitch bifurcation diagram of the 'kinematic squirrel', we see a Hopf bifurcation for a critical $\bar{\theta}$ near 0. We can see that $d < 0$ (eigenvalues going from right half-plane to left half-plane as $\theta - \bar{\theta}$ increases through zero). The numerically determined unstable limit cycle exists for $\theta > \bar{\theta}$, which is consistent with $a > 0$, so we predict that calculating (6.39) will give $a > 0$. We also predict that the limit cycle will have a period of approximately $T = \frac{2\pi}{\omega}$ where ω is given from (6.33), and that the radius of the limit cycle in the (x, y) plane, close to the pitch value $\bar{\theta}$, is given by

$$\rho = \sqrt{-\tfrac{d}{a}(\theta - \bar{\theta})} \tag{6.42}$$

Notice that the dependence of ρ on the constants a and d, as well as distance away from the bifurcation point, $(\theta - \bar{\theta})$, reveal how 'quickly' the size of the limit cycle grows. The amplitude of

the limit cycle in terms of glide angle γ is provided from (6.35) as,

$$\rho_\gamma = 2C_L\rho = 2C_L\sqrt{-\tfrac{d}{a}(\theta - \bar{\theta})} \tag{6.43}$$

6.3 Stable node case

If $\bar{\tau} < 0$ and $\bar{\tau}^2 - 4\bar{\Delta} > 0$ (so $\sqrt{\bar{\tau}^2 - 4\bar{\Delta}} > 0$), then we have two real, and negative, eigenvalues. The larger magnitude eigenvalue is

$$\lambda_{ss} = \frac{\bar{\tau} - \sqrt{\bar{\tau}^2 - 4\bar{\Delta}}}{2} = \tfrac{1}{2}\bar{v}^* \left(-C_L' - 3C_D - \sqrt{(C_D - C_L')^2 - 8C_L(C_L - C_D')} \right), \tag{6.44}$$

and the smaller magnitude eigenvalue is

$$\lambda_s = \frac{\bar{\tau} + \sqrt{\bar{\tau}^2 - 4\bar{\Delta}}}{2} = \tfrac{1}{2}\bar{v}^* \left(-C_L' - 3C_D + \sqrt{(C_D - C_L')^2 - 8C_L(C_L - C_D')} \right), \tag{6.45}$$

so $\lambda_{ss} < \lambda_s < 0$, where '$s$' denotes *stable* and '$ss$' denotes *super stable*. Let the corresponding eigenvectors be $\mathbf{e}_{ss}$ and $\mathbf{e}_s$, respectively, understood as column vectors.

Now $\bar{\tau} < 0$ implies that

$$C_L' > -3C_D$$

, and $\bar{\tau}^2 - 4\bar{\Delta} > 0$ implies that

$$(C_D - C_L')^2 > 8C_L(C_L - C_D')$$

We can solve for $\mathbf{e}_s$, since it will give us a local approximation of the *terminal velocity manifold* described in the text. All we want is the slope $\bar{m}$ (in (ψ, r) coordinates), so we let $\mathbf{e}_s = [-1, -\bar{m}]^T$. From the eigenvector formula

$$\mathbf{A}\mathbf{e}_s = \lambda_s \mathbf{e}_s$$

where

$$\mathbf{A} = \begin{bmatrix} a & b \\ c & d \end{bmatrix} \tag{6.46}$$

we have

$$\bar{m} = \frac{\lambda_s - a}{b} \tag{6.47}$$

and using (6.22) and (6.53), we get

$$a = \bar{v}^* \left[-C_L' - C_D \right], \quad b = [-2C_L]$$

and thus,

$$\bar{m} = \frac{\bar{v}^*}{4C_L} \left(C_D - C_L' - \sqrt{(C_D - C_L')^2 - 8C_L(C_L - C_D')} \right) \tag{6.48}$$

We want the slope m in $(\bar{v}_x, \bar{v}_z)$ coordinates, so, using the relationship between the cartesian and polar coordinates,

$$\begin{aligned}\bar{v}_x &= \quad \bar{v}\cos\gamma \\ \bar{v}_z &= -\bar{v}\sin\gamma\end{aligned}$$

we write the transformation between local vectors,

$$\begin{bmatrix} d\bar{v}_x \\ d\bar{v}_z \end{bmatrix} = \begin{bmatrix} -\bar{v}^*\sin\gamma^* & \cos\gamma^* \\ -\bar{v}^*\cos\gamma^* & -\sin\gamma^* \end{bmatrix} \begin{bmatrix} d\psi \\ dr \end{bmatrix} \tag{6.49}$$

and letting $dr = \bar{m}\, d\psi$, we get the slope of the terminal velocity manifold,

$$m = \frac{d\bar{v}_z}{d\bar{v}_x} = \frac{\bar{v}^*\cos\gamma^* + \bar{m}\sin\gamma^*}{\bar{v}^*\sin\gamma^* - \bar{m}\cos\gamma^*} \tag{6.50}$$

with $\bar{m}$ as in (6.56). Note, this is the *local* slope of the terminal velocity manifold, as evaluated at the stable node point. The slope may change, i.e., the manifold may be curved, as explored in the next case.

For completeness, we also compute the eigenvector $\mathbf{e}_{ss} = [-1, -\bar{n}]^T$, and get

$$\bar{n} = \frac{\bar{v}^*}{4C_L}\left(C_D - C_L' + \sqrt{(C_D - C_L')^2 - 8C_L(C_L - C_D')}\right) \tag{6.51}$$

6.4 Saddle case

If $\bar{\Delta} < 0$, so $\bar{\Delta} = -|\bar{\Delta}|$, then $\sqrt{\bar{\tau}^2 - 4\bar{\Delta}} = \sqrt{\bar{\tau}^2 + 4|\bar{\Delta}|} > |\bar{\tau}|$, then we have two real eigenvalues, one negative (λ_s) and one positive (λ_u). The negative eigenvalue is

$$\lambda_s = \frac{\bar{\tau} - \sqrt{\bar{\tau}^2 - 4\bar{\Delta}}}{2} = \tfrac{1}{2}\bar{v}^*\left(-C_L' - 3C_D - \sqrt{(C_D - C_L')^2 - 8C_L(C_L - C_D')}\right), \tag{6.52}$$

and the positive eigenvalue is

$$\lambda_u = \frac{\bar{\tau} + \sqrt{\bar{\tau}^2 - 4\bar{\Delta}}}{2} = \tfrac{1}{2}\bar{v}^*\left(-C_L' - 3C_D + \sqrt{(C_D - C_L')^2 - 8C_L(C_L - C_D')}\right), \tag{6.53}$$

Let the corresponding eigenvectors be $\mathbf{e}_s$ and $\mathbf{e}_u$, respectively, understood as column vectors.

We can solve for $\mathbf{e}_u$, since it will give us a local approximation of the *terminal velocity manifold* described in the text. All we want is the slope $\bar{m}$ (in (ψ, r) coordinates), so we let $\mathbf{e}_u = [-1, -\bar{m}]^T$. From the eigenvector formula

$$\mathbf{A}\mathbf{e}_u = \lambda_u \mathbf{e}_u$$

where

$$\mathbf{A} = \begin{bmatrix} a & b \\ c & d \end{bmatrix} \tag{6.54}$$

we have

$$\bar{m} = \frac{\lambda_u - a}{b} \tag{6.55}$$

and using (6.22) and (6.53), we get

$$a = \bar{v}^* \left[-C_L' - C_D \right], \quad b = [-2C_L]$$

and thus,

$$\bar{m} = \frac{\bar{v}^*}{4C_L} \left(C_D - C_L' - \sqrt{(C_D - C_L')^2 - 8C_L(C_L - C_D')} \right) \tag{6.56}$$

We want the slope m in $(\bar{v}_x, \bar{v}_z)$ coordinates, so, using the relationship between the cartesian and polar coordinates,

$$\begin{aligned} \bar{v}_x &= \quad \bar{v} \cos\gamma \\ \bar{v}_z &= -\bar{v} \sin\gamma \end{aligned} \tag{6.57}$$

we write the transformation between local vectors,

$$\begin{bmatrix} d\bar{v}_x \\ d\bar{v}_z \end{bmatrix} = \begin{bmatrix} -\bar{v}^* \sin\gamma^* & \cos\gamma^* \\ -\bar{v}^* \cos\gamma^* & -\sin\gamma^* \end{bmatrix} \begin{bmatrix} d\psi \\ dr \end{bmatrix} \tag{6.58}$$

and letting $dr = \bar{m}\, d\psi$, we get the slope of the terminal velocity manifold,

$$m = \frac{d\bar{v}_z}{d\bar{v}_x} = \frac{\bar{v}^* \cos\gamma^* + \bar{m} \sin\gamma^*}{\bar{v}^* \sin\gamma^* - \bar{m} \cos\gamma^*} \tag{6.59}$$

with $\bar{m}$ as in (6.56). Again, this is the *local* slope of the terminal velocity manifold, as evaluated at the saddle point, and may be different from the local slope of the terminal velocity manifold as evaluated at the stable node, if the manifold is curved.

For completeness, we also compute the eigenvector $\mathbf{e}_s = [-1, -\bar{n}]^T$, and get

$$\bar{n} = \frac{\bar{v}^*}{4C_L} \left(C_D - C_L' + \sqrt{(C_D - C_L')^2 - 8C_L(C_L - C_D')} \right) \tag{6.60}$$

Higher order approximation of terminal velocity manifold. Define the matrix $\mathbf{P}$ as

$$\begin{aligned} \mathbf{P} &= [\mathbf{e}_u \;\; \mathbf{e}_s] \\ &= \begin{bmatrix} -1 & -1 \\ -\bar{m} & -\bar{n} \end{bmatrix} \end{aligned}$$

so $\mathbf{e}_u$ is the first column of $\mathbf{P}$ and $\mathbf{e}_s$ is the second column of $\mathbf{P}$.

This matrix defines a linear transformation to the eigenbasis (x, y) via

$$\begin{bmatrix} \psi \\ r \end{bmatrix} = \mathbf{P} \begin{bmatrix} x \\ y \end{bmatrix}$$

so the x coordinate is along the $\mathbf{e}_u$ direction and the y coordinate is along the $\mathbf{e}_s$ direction. Note that

$$\begin{aligned} \psi &= -x - y \\ r &= -\bar{m}x - \bar{n}y \end{aligned} \tag{6.61}$$

and

$$\mathbf{P}^{-1} = \frac{1}{\bar{m} - \bar{n}} \begin{bmatrix} \bar{n} & -1 \\ -\bar{m} & 1 \end{bmatrix} \tag{6.62}$$

Considering (6.18), we have

$$\begin{bmatrix} x' \\ y' \end{bmatrix} = \underbrace{\mathbf{P}^{-1}\mathbf{A}\mathbf{P}}_{\mathbf{\Lambda}} \begin{bmatrix} x \\ y \end{bmatrix} + \mathbf{P}^{-1}\mathbf{F}(x, y) \tag{6.63}$$

where $\mathbf{\Lambda}$ is the diagonalized matrix,

$$\mathbf{\Lambda} = \begin{bmatrix} \lambda_u & 0 \\ 0 & \lambda_s \end{bmatrix}$$

and where care must be taken to calculate the second-order terms, $\mathbf{P}^{-1}\mathbf{F}(x, y)$, in terms of x and y, where $\mathbf{F}(x, y)$ is given as in (6.19)-(6.21).

We will re-write the nonlinear terms, defining $\mathbf{f}(x, y) = \mathbf{P}^{-1}\mathbf{F}(-x - y, -\bar{m}x - \bar{n}y)$, so

$$\mathbf{f}(x, y) = \frac{1}{\bar{m} - \bar{n}} \begin{bmatrix} \bar{n} & -1 \\ -\bar{m} & 1 \end{bmatrix} \begin{bmatrix} a_1x^2 + a_2xy + a_3y^2 \\ b_1x^2 + b_2xy + b_3y^2 \end{bmatrix} + \mathcal{O}(3)$$

where

$$
\begin{aligned}
a_1 &= a^1 + b^1\bar{m} + c^1\bar{m}^2 \\
a_2 &= 2a^1 + b^1(\bar{m} + \bar{n}) + 2c^1\bar{m}\bar{n} \\
a_3 &= a^1 + b^1\bar{n} + c^1\bar{n}^2 \\
b_1 &= a^2 + b^2\bar{m} + c^2\bar{m}^2 \\
b_2 &= 2a^2 + b^2(\bar{m} + \bar{n}) + 2c^2\bar{m}\bar{n} \\
b_3 &= a^2 + b^2\bar{n} + c^2\bar{n}^2 \\
a^1 &= \tfrac{\bar{v}^*}{2}\left[-C_L - C_L''\right] \\
b^1 &= \left[C_D - C_L'\right] \\
c^1 &= \tfrac{1}{\bar{v}^*}[C_L] \\
a^2 &= \tfrac{\bar{v}^{*2}}{2}\left[-C_D - C_D''\right] \\
b^2 &= 2\bar{v}^*[-C_D'] \\
c^2 &= [-C_D]
\end{aligned}
$$

We will refer to the components of $\mathbf{f}$ as (f, g).

The resulting equation now has the form,

$$
\begin{bmatrix} x' \\ y' \end{bmatrix} = \begin{bmatrix} \lambda_u & 0 \\ 0 & \lambda_s \end{bmatrix} \begin{bmatrix} x \\ y \end{bmatrix} + \begin{bmatrix} f(x,y) \\ g(x,y) \end{bmatrix} \tag{6.64}
$$

where

$$
\begin{aligned}
f(x,y) &= c_1x^2 + c_2xy + c_3y^2 + \mathcal{O}(3) \\
g(x,y) &= d_1x^2 + d_2xy + d_3y^2 + \mathcal{O}(3)
\end{aligned} \tag{6.65}
$$

where

$$
\begin{aligned}
c_i &= \tfrac{1}{\bar{m}-\bar{n}}(\ \ \bar{n}a_i - b_i) \\
d_i &= \tfrac{1}{\bar{m}-\bar{n}}(-\bar{m}a_i + b_i)
\end{aligned}
$$

We will end up with the expansion about the equilibrium in a form where we can now calculate the terminal velocity manifold. We re-write (6.64) as,

$$
\begin{aligned}
x' &= \lambda_u x + f(x,y) \\
y' &= \lambda_s y + g(x,y)
\end{aligned} \tag{6.66}
$$

where $f(x, y)$ is second-order and higher in x and y, as is $g(x, y)$.

We assume the terminal velocity manifold is given by $y = h(x)$, where $h(x)$ has the Taylor series

expansion form,

$$h(x) = ax^2 + bx^3 + \mathcal{O}(x^4) \tag{6.67}$$

We can solve for the coefficients a and b by taking the time derivative of $y = h(x)$, which gives

$$\frac{\partial h}{\partial x} x' - y' = 0$$

i.e.,

$$\frac{\partial h}{\partial x} \left[\lambda_u x + f(x, h(x))\right] - \left[\lambda_s h(x) + g(x, h(x))\right] = 0$$

and equating like powers of x,

$$(2ax + 3bx^2 + \mathcal{O}(x^3)) \left[\lambda_u x + c_1 x^2 + \mathcal{O}(x^3)\right] - \left[\lambda_s a x^2 + d_1 x^2 + \mathcal{O}(x^3)\right] = 0$$

i.e.,

$$\left[a(2\lambda_u - \lambda_s) - d_1\right] x^2 = 0$$

so

$$a = \frac{d_1}{(2\lambda_u - \lambda_s)}$$

Thus, to a second-order approximation in the (x, y) coordinates, the terminal velocity manifold is expressed as

$$y = h(x) = \frac{d_1}{(2\lambda_u - \lambda_s)} x^2 + \mathcal{O}(x^3)$$

thus, in general the manifold will be curved. To get the curvature up through third-order terms, we need b, so we would have to have $\mathbf{f}(x, y)$ calculated up to the third-order terms. We note that this whole process can be automated using automatic power series expansion tools [10].

To get the terminal velocity manifold in the original $(\bar{v}_x, \bar{v}_z)$ coordinates, we use (6.61), (6.1), and (6.57), to get a parametric curve,

$$\begin{aligned} \bar{v}_x(u) = &\quad (\bar{v}^* - \bar{m}u - \bar{n}h(u)) \cos(\gamma^* - u - h(u)) \\ \bar{v}_z(u) = &-(\bar{v}^* - \bar{m}u - \bar{n}h(u)) \sin(\gamma^* - u - h(u)) \end{aligned} \tag{6.68}$$

parametrized by a curvilinear coordinate u which we take to be in some interval $I \subset \mathbb{R}$, where the function h is as in (6.67).

We can determine the lowest order non-linear approximation of the vector field *along the 1-dimensional terminal velocity manifold*, as

$$\begin{aligned} u' &= \lambda_u u + f(u, h(u)) \\ &= \lambda_u u + c_1 u^2 + \mathcal{O}(u^3) \end{aligned} \tag{6.69}$$

where we are using u as a curvilinear (arc-length) coordinate along the terminal velocity manifold. This is the analytical formula for the 'speed' (actually, acceleration) along the terminal velocity

curve vs. location along that curve. This tells us that a second equilibrium point (stable) will show up along the terminal velocity manifold at $u = -\lambda_u/c_1$, which is an approximation of where the stable node is located.

It is interesting that the local approximation of the dynamics around the saddle point can imply the existence of the stable point. Also noteworthy is the fact that the terminal velocity manifold constructed from the saddle point to the stable node is a heteroclinic trajectory (backward asymptotic to the saddle point and forward asymptotic to the stable node) along which the relative speed varies according to (6.69).

To find out what role the shape of the terminal velocity manifold plays in modifying the vector field along it, we must consider third-order terms in (6.18), which would give us

$$\begin{aligned} u' &= \lambda_u u + f_2(u, h(u)) + f_3(u, h(u)) + \mathcal{O}(u^4) \\ &= \lambda_u u + c_1 u^2 + c_2 a u^3 + k_1 u^3 + \mathcal{O}(u^4) \\ &= \lambda_u u + c_1 u^2 + \left[c_2 \tfrac{d}{(2\lambda_u - \lambda_s)} + k_1 \right] u^3 + \mathcal{O}(u^4) \end{aligned} \tag{6.70}$$

where $f_2(x, y) = c_1 x^2 + c_2 xy + c_3 y^2$ and $f_3(x, y) = k_1 x^3 + k_2 x^2 y + k_3 x y^2 + k_4 y^3$ are the second and third order terms in the x' equation of (6.66), respectively.

Note that

$$k_1 = \tfrac{1}{\bar{m} - \bar{n}} (\bar{n} \tilde{a}_1 - \tilde{b}_1)$$

where

$$\begin{aligned} \tilde{a}_1 &= -(A_1 + A_2 \bar{m} + A_3 \bar{m}^2 + A_4 \bar{m}^3) \\ \tilde{b}_1 &= -(B_1 + B_2 \bar{m} + B_3 \bar{m}^2 + B_4 \bar{m}^3) \end{aligned}$$

and where the A_i and B_i come from the third-order coefficients in (6.20) and (6.21), respectively,

$$\begin{aligned} A_1 &= \tfrac{\bar{v}^*}{6} [C_D - C_L'''] \\ A_2 &= \tfrac{1}{2} [C_L - C_L''] \\ A_3 &= \tfrac{1}{\bar{v}^*} [-C_D] \\ A_4 &= \tfrac{1}{\bar{v}^{*2}} [-C_L] \\ B_1 &= \tfrac{\bar{v}^{*2}}{6} [-C_L - C_D'''] \\ B_2 &= \bar{v}^* [-C_D''] \\ B_3 &= \tfrac{1}{2} [-C_D'] \\ B_4 &= 0 \end{aligned}$$

We note that the third-order coefficient b is given by

$$b = \frac{g_1 - a(2c_1 - d_2)}{3\lambda_u - \lambda_s}$$

where

$$g_1 = \frac{1}{\bar{m}-\bar{n}}(-\bar{m}\tilde{a}_1 + \tilde{b}_1)$$

6.5 Terminal velocity manifold as slow manifold

In the previous sections, we have looked for local approximations of the terminal velocity manifold near an equilibrium point, building off of the invariant manifold structure near the equilibrium. However, we may be able to consider another, more global approach, inspired by singular perturbation theory [7]. In some systems, one can identify a fast variable and a slow variable when a small parameter appears in one of the ODEs. The dynamics of the fast variable quickly collapse onto a lower dimensional manifold on which the dynamics evolve more slowly (the slow variable). In the re-scaled gliding equations of motion for $(\bar{v}_x, \bar{v}_z)$, no slow-fast structure can be identified in the equations themselves (i.e., there is no natural choice of a small parameter), yet a slow manifold appears to exist. While we do not consider it here, there may methods to obtain the approximate slow manifold [11, 12], based on the extended zero derivative principle, even if fast and slow variables have not been identified.

6.6 Acceleration along the terminal velocity manifold

In figure 5bii of the text, we include an inset showing the approximation of the terminal velocity manifold in the vicinity of the saddle point equilibrium. Below we show the acceleration magnitude of the glider along the manifold using both the 2^{nd}-order and 3^{rd}-order approximations.

References

[1] Kristin L Bishop. The relationship between 3-D kinematics and gliding performance in the southern flying squirrel, *Glaucomys volans*. *J. Exp. Biol.*, 209:689–701, 2006. doi: 10.1242/jeb.02062.

[2] Joseph W. Bahlman, Sharon M. Swartz, Daniel K. Riskin, and Kenneth S. Breuer. Glide performance and aerodynamics of non-equilibrium glides in northern flying squirrels (*Glaucomys sabrinus*). *J. R. Soc. Interface*, 10(20120794), 2013. doi: 10.1098/rsif.2012.0794.

[3] Haym Benaroya, Seon Mi Han, and Mark Nagurka. *Probability Models in Engineering and Science*, volume 193. CRC Press, 2005.

[4] Alex Papanicolaou. Taylor approximation and the delta method, 2009.

[5] B. F. Mettler. Extracting micro air vehicles aerodynamic forces and coefficients in free flight using visual motion tracking techniques. *Exp. Fluids*, 49:557–569, 2010. doi: 10.1007/s00348-009-0803-6.

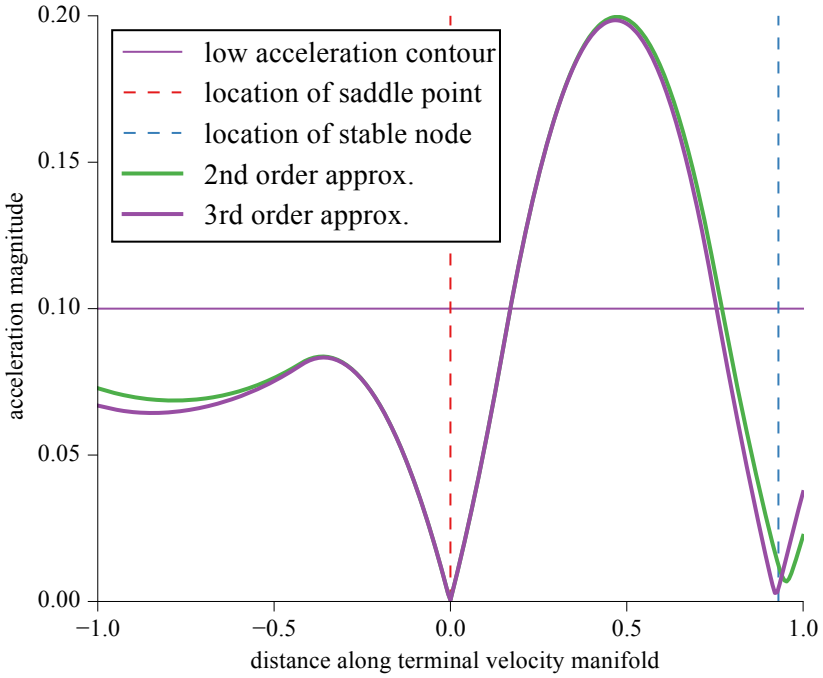

Figure 3: Acceleration along the terminal velocity manifold for the airfoil snake at a pitch angle of $\theta = 5°$

.

[6] Daniel V. Uhlig and Michael S. Selig. Determining aerodynamic characteristics of a micro air vehicle using motion tracking. *J. Aircr.*, 50:1481–1490, 2013. doi: 10.2514/1.C031996.

[7] Steven H. Strogatz. *Nonlinear Dynamics and Chaos: With Applications to Physics, Biology, Chemistry, and Engineering*. Perseus Books Publishing, LLC, 2001.

[8] Stephen Wiggins. *Introduction to Applied Nonlinear Dynamical Systems and Chaos*, volume 2. Springer Science & Business Media, 2003.

[9] J.E. Marsden and M. McCracken. *The Hopf Bifurcation and Its Applications*. Springer-Verlag, New York, Heidelberg, Berlin, 1976.

[10] G. Gómez, W. S. Koon, M. W. Lo, J. E. Marsden, J. Masdemont, and S. D. Ross. Connecting orbits and invariant manifolds in the spatial three-body problem. *Nonlinearity*, 17:1571–1606, 2004.

[11] Morten Brøns. An iterative method for the canard explosion in general planar systems. *Discrete and Continuous Dynamical Systems Supplement 2013*, pages 77–83, 2013.

[12] M. Brøns and K. Uldall Kristiansen. On the approximation of the canard explosion point in epsilon-free systems. *ArXiv e-prints*, 2015.